

## Master-Thesis

# INVESTIGATION OF PARTICLE PRECIPITATION EVENTS IN THE IONOSPHERIC D REGION AND BELOW

**Submitted on:** 27 October, 2021

**Submitted By:** Archana Vijayalekshmi Harikumar  
Born on October 21, 1992  
in Kerala, India  
Mat Nr. 348063

**Supervisors:** Prof.Dr. Ing.habil. Andreas Ahrens  
Dr. Ing. Toralf Renkwitz

## Abstract

Ionosphere is the ionized part of earth's atmosphere which spreads over 60km. to more than 250km altitude. Ionization in this region is preliminarily due to the solar radiation. Studies shows that there are regions where the density of electrons changes with altitude, referred as the D, E, Es, F1 and F2 layers. These layers are normally identified by using HF radars. Several decades ago, a "C"-layer around 50-60km altitude has been found, but which is not widely accepted. Medium frequency radars are used for the identification of this layer. A 3.17 MHz medium frequency radar is used in IAP, which is operated in Northern Norway. This radar is very sensitive to enhanced ionization, so that it can detect even the partial reflections caused by particle precipitation from even 50km altitude.

In this work, layers around 60km altitude caused by precipitating particles with low energy are detected. The particle precipitation is observed by spectral analysis. Also, such layers occurring at these altitudes, which are not related to particle precipitation is observed. The analysis is done by using both the pre analyzed data and the original radar raw data. The raw data is further used for the analysis of broadening of the spectral arc due the horizontal wind.

## Abstrakt

Die Ionosphäre ist der ionisierte Teil der Erdatmosphäre, der sich über eine Höhe von 60 km bis zu mehr als 250 km erstreckt. Die Ionisierung in dieser Region ist in erster Linie auf die Sonneneinstrahlung zurückzuführen. Studien zeigen, dass es Regionen gibt, in denen sich die Elektronendichte mit der Höhe ändert, die so genannten D, E, Es, F1 und F2-Schichten. Diese Schichten werden normalerweise mit Hilfe von HF-Radargeräten identifiziert. Vor einigen Jahrzehnten wurde eine "C"-Schicht in 50-60 km Höhe gefunden, die jedoch nicht allgemein anerkannt ist. Für die Identifizierung dieser Schicht werden Mittelfrequenzradare eingesetzt. Ein Mittelfrequenzradar wird im IAP eingesetzt, das in Nordnorwegen betrieben wird. Dieses Radar ist sehr empfindlich gegenüber verstärkter Ionisierung, so dass es sogar die durch Partikelniederschlag verursachten Teilreflexionen aus 50 km Höhe erkennen kann.

In dieser Arbeit werden Schichten um 60 km Höhe, die durch niederschlagende Partikel mit niedriger Energie verursacht werden, erfasst. Der Partikelniederschlag wird durch Spektralanalyse beobachtet. Außerdem werden in diesen Höhen Schichten beobachtet, die nicht mit dem Partikelniederschlag in Verbindung stehen. Für die Analyse werden sowohl die voranalysierten Daten als auch die ursprünglichen Radarrohdaten verwendet. Die Rohdaten werden weiterhin für die Analyse der Verbreiterung des Spektralbogens aufgrund des horizontalen Windes verwendet.

---

**Content**

<b>Abstract</b> .....	2
<b>1 Introduction</b> .....	6
1.1 Motivation .....	9
<b>2 Instrumentation</b> .....	12
2.1 Architecture of Saura MF radar .....	13
2.2 Advantages of Saura MF radar .....	15
<b>3 Particle precipitation events</b> .....	16
3.1 Overview .....	16
3.2 Observation of particle precipitation events by Saura MF .....	18
3.2.1 Analysis of Quiet and disturbed days .....	20
3.3 Selection of ILME events from DBS data .....	22
3.4 Statistics of Particle precipitation occurrence .....	25
3.4.1 Special Case .....	27
3.5 Comparison of the observations with previous analysis .....	28
3.5.1 Geomagnetic indices .....	29
<b>4 Investigation of ionospheric layers by analyzing radar raw data</b> .....	31
4.1 Analysis procedure .....	33
4.1.1 Data migration facility (DMF) .....	34
4.2 Calculation of spectra using python .....	37
4.3 Preparation of the data set .....	38
4.3.1 Unusual echoes seen in spectral analysis .....	41
4.4 Statistics .....	42
4.5 Cause of occurrence of isolated layers .....	44
4.5.1 Ground clutter .....	44
4.5.2 Radiation sources .....	48
<b>5 Broadening of spectral arc</b> .....	51
5.1 Wind measurement technique .....	53
5.2 Calculation and Comparison of horizontal wind on spectra .....	55
5.3 Potential errors in wind measurement .....	57
5.3.1 Solution to wind correction .....	59

<b>6 Conclusions and summary .....</b>	<b>60</b>
<b>List of figures .....</b>	<b>62</b>
<b>List of Tables .....</b>	<b>65</b>
<b>List of Abbreviations.....</b>	<b>66</b>
<b>List of references .....</b>	<b>68</b>
<b>Acknowledgment.....</b>	<b>71</b>
<b>Statement of Authorship.....</b>	<b>72</b>

## 1 Introduction

The atmosphere that surrounds the Earth is a very complex system. It is comprised of gases, which is bounded by gravity. The density and composition of the gases and their physical properties changes with increase in height, forming regions with distinct properties.

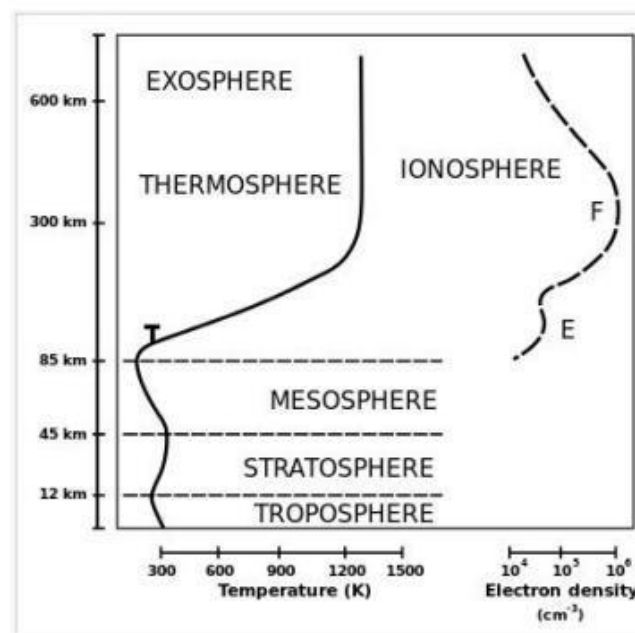


**Figure 1** : Representative temperature and electron density as a function of altitude. [1]

Based on various criteria's, the atmosphere can be divided into different layers. The major parameters used for defining the layers are temperature, composition, and the electron density. The temperature distribution profile determines the layers troposphere, stratosphere, mesosphere thermosphere and exosphere and electron density determines the ionosphere. The lowest layer is the troposphere which extends up to 12km, followed by stratosphere, Mesosphere Thermosphere. A further region, beginning from about 500 km above the Earth's surface, is the exosphere. Each layers have different lapse rate, defining the rate of change in temperature with height.

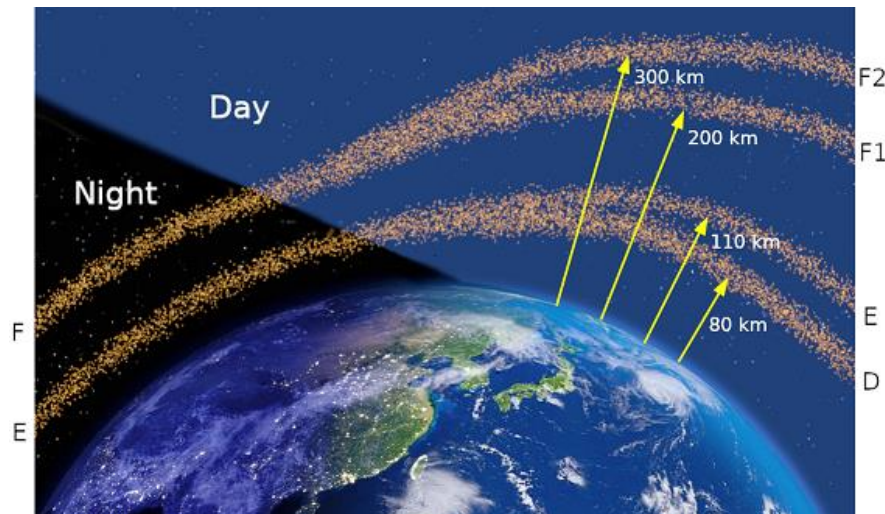


**Figure 2:** Division of ionosphere regions by electron density. [1]

The ionosphere represents the upper part of the atmosphere, where the electrically charged particles are present. It absorbs the incoming solar radiation that is the high energy X rays and UV rays from the sun and creates the electron ion pairs resulting in a weakly ionized plasma. Its behavior is determined by the solar and geomagnetic activities. The ionosphere increases in thickness and moves closer to the Earth during daylight and rises at night. Also, the boundaries of these layers varies during season to season. In the morning time more ions are created because of the presence of sun and during night recombination process happens in the absence of sunlight and the ion density drops. Hence, during night the lower part of ionosphere disappears entirely and the upper part gets weaker. It allows certain frequencies of radio communication over a greater range. Generally, ionosphere extends from 50 km altitude to more than 500 km.

The layers of ionosphere is classified into D, E, Es, F1 and F2. The F region starts from an altitude range of 150 km. The altitude range from 90 km refers to E layer and the region below 90 km is named the D layer, which is the layer typically observed in IAP. D region normally starts from 60 km and the echo power intensifies and maximize near 85-90 km altitude. Sometimes we can detect signals also around 50-60 km altitude and this is referred as C layer. Decades ago scientists postulated that, C layer exists but some people opposed this.

This layer is difficult to detect as it needs a powerful system to see and may be this is the primary reason why people refused to believe this concept. In IAP a medium frequency radar is used to see this C layer.

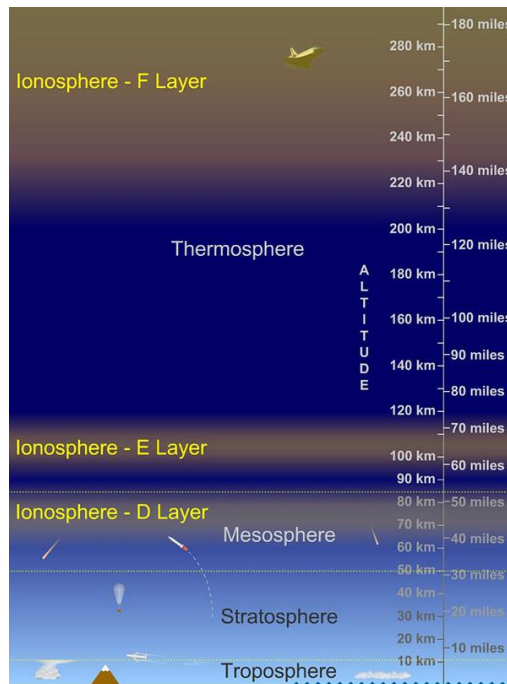


**Figure 3** : Regions of the ionosphere showing the D, E and F layer. [2]

This project focuses mainly on low altitude ionosphere ranges from 50 to 60 km altitudes, which is the D region and below. The data for many years are checked and looked for presence of the C layers and also the relation of these layers to the atmospheric conditions are analyzed. For instance, checking whether the solar radiations like X-rays and UV were very intense during the presence of the C layer or not. Also large geomagnetic storm caused by solar flares and coronal mass ejection (CME) from the sun is analyzed in this study. The magnetic belts are present especially around and over the polar regions, where the radar is located.

Sometimes the particle precipitation due to aurora are often intensely seen at high altitudes and further down, we can see the precipitation of electrons and protons down to 50 km altitude and so there is probably a relation of these events to the layers. In this thesis, these particle precipitation events is connected to the layers.

These events occur fairly often mainly around the equinoxes. The northern light is seen in lower atmosphere around spring and autumn, we can visually see these around 100-150 km altitude and they leave a clear signature in the radar data.

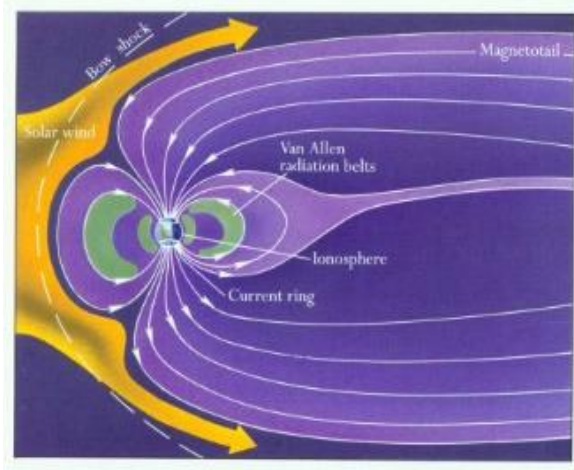


**Figure 4:** Charged electrons in Earth's magneto tail.  
[3]



**Figure 5:** Northern light seen in western Canada.  
[4]

## 1.1 Motivation

Several decades ago, experimental results have indicated the existence of a layer of ionization below the D-region of the ionosphere. According to Rasmussen et al.[1980], A constant thick layer is seen at 63km altitude after sunrise and before sunset hours, which is shown in Figure 6. They claim that the low altitude ionization may indeed be a C layer, but does not give a clear idea about the persistence of this layer. Scientist introduces this phenomena related to chemistry of the atmosphere [Bain and May, 1967].According to Nicolet et al.[1960], the low altitude layer occurred during day time is due to the combined action of cosmic rays and solar radiation. During night, the electrons produced by the cosmic rays combines with the neutral particle to form negative ions. The electrons, emitted by the negative ions due to solar radiation by photodetachment causes an electron population. However, it does not interact with VLF wave. These electrons form a band of ionization, which extends well below the D region of the ionosphere. The low altitude ionization based on electron profile discontinuity named as C layer by Krasnushkin [1962].

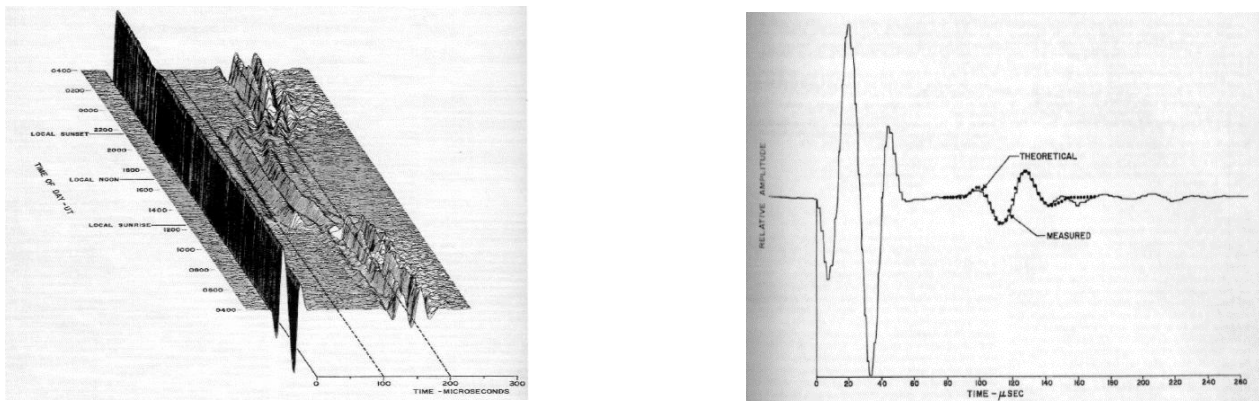


**Figure 6:** Pulse reflected data of 28/12/1972(left) and 6km thick layer of ionization located at 63km altitude.[5]

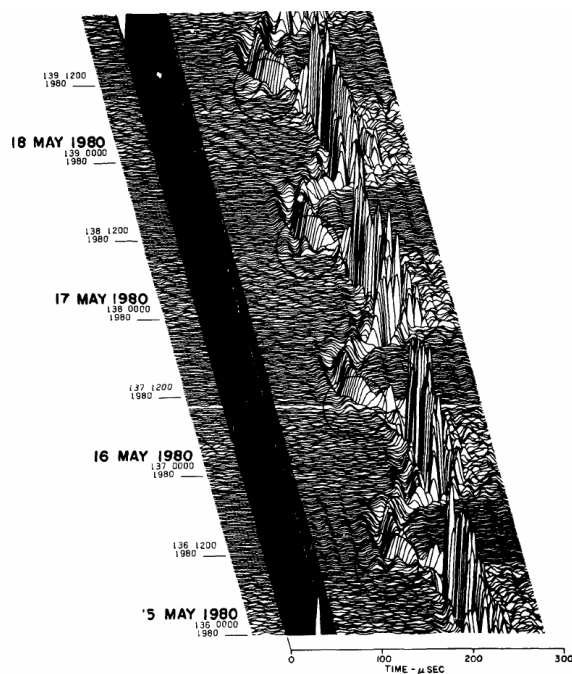


**Figure 7:** Data obtained at camboriu showing weak reflections (circled areas) from altitude below the normal D-Region. [5]

The distinct layers in the ionosphere can be observed by particle precipitation events. The experiment for the identification of energetic particle precipitation, by understanding the electron density variations using a medium frequency radar is conducted in IAP. During precipitation events the altitude as low as 50 km can be significantly ionized causing apparent layers [T. Renkwitz et al. 2017]. The Figure 8 shows an example of the D, E, F layers as seen by the Saura MF radar. In this, the F layer is seen in between 200-300 km, the E region is seen from 150 km altitude and below that is the D region from 60-90 km altitude.

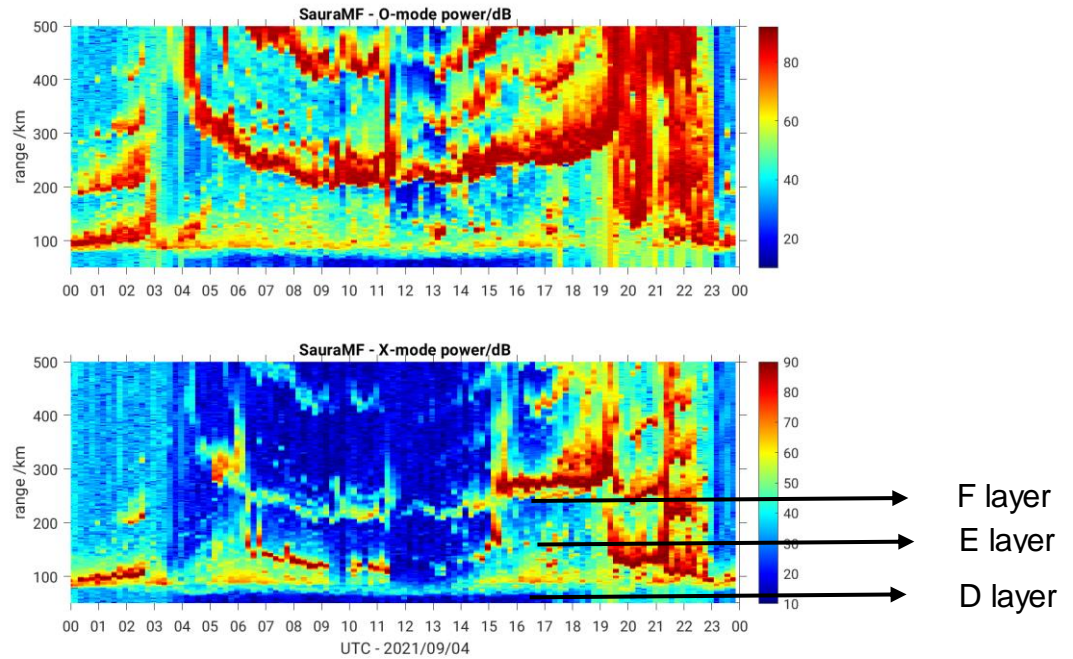


**Figure 8:** Data obtained from Saura MF radar showing the D, E, F regions on 4<sup>th</sup> September 2021

Energetic particles like protons, heavier ions and electrons that precipitate in the atmosphere comes from different sources. These particles comes directly from the sun in large solar particle events (SPEs), from the aurora, from the radiation belts during geomagnetic storms and sub storms, or from outside the solar system. The Galactic cosmic rays (GCRs) or other energetic particles enters the Earth's atmosphere and react with the chemical species in the atmosphere. The high kinetic energy of these particle causes ionization of neutral constituents and leads to the additional production of HO<sub>x</sub> and NO<sub>x</sub>, which accelerate the ozone depletion (O<sub>3</sub>) cycle in the middle atmosphere.

The effects of energetic particle precipitation on observation by the medium frequency radars are very rarely reported. Also, the precipitation of highly energetic solar proton events are clear. The goal of this thesis is to investigate precipitation events associated with particles having low energy, thereby analyzing the C region and D region of the ionosphere.

## 2 Instrumentation

Radio detection and ranging abbreviated as RADAR, are used for the measurement and observation of atmosphere. It radiates electromagnetic waves, which will be reflected or scattered by targets. The nature of the echoes provides the information about the targets. The range to the target is often calculated by taking the time required for the radiated pulse from the radar for its to and fro travel. Angular location of the target is observed with a narrow beam emitted from the directive antenna (AOA, Angle of arrival measurement of the echo signal). The Doppler shift gives information about the location of a moving target. Target size and shape can be calculated by improving the radar resolution. The magnitude of the returned echoes to the receiver gives an idea about the target size and the direction of received echoes gives the information of target shape. Radars was originally developed for the military application. However, it is used for civil applications and remote sensing of the environment, especially the weather.

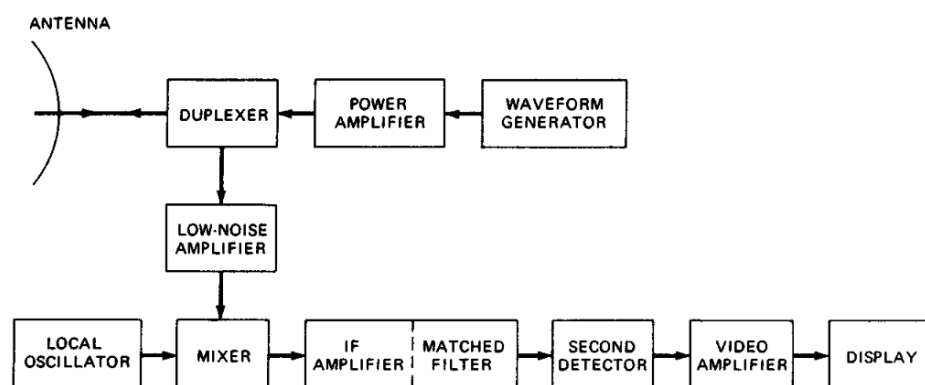


**Figure 9** : Simple block diagram of a radar employing a power amplifier, transmitter and a receiver [10].

Radar can operate in a wide frequency range from several megahertz to gigahertz (MHz to GHz) region of the spectrum. 300-3000 kHz is considered as medium frequency, 3-30 MHz is considered as High frequency (HF), 30-300 MHz is very high frequency (VHF), and 300-3000 MHz is ultrahigh frequency (UHF) and so on. The MST (mesosphere-stratosphere-troposphere) radar technique is used for the observation of middle atmosphere. This technique gives an excellent time and space resolution and is used for observing winds, waves, turbulence and atmospheric stability over the altitude till 100km [Balsley and Gage, 1980].

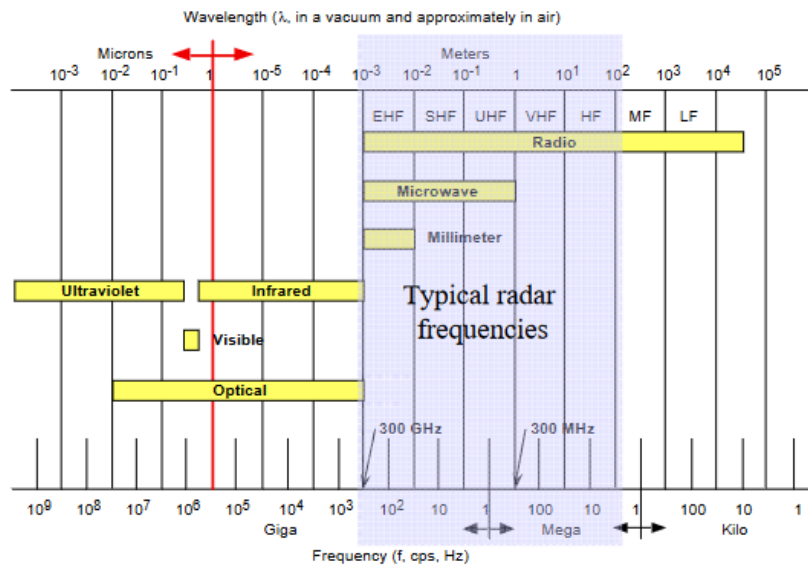


Figure 10 : The Electromagnetic spectrum [12]

## 2.1 Architecture of Saura MF radar

This study aims on the middle atmosphere mainly in 50-90 km altitude. The radar target in this region are plasma irregularities occurred due to solar and geomagnetic activities and dynamics like wave activities. The 3.17MHz medium frequency Saura radar, built in July 2002 is used for the study of energetic particle precipitation in lower ionospheric region. The radar was installed 20 km south of the Andoya Space Centre in Northern Norway at 69.1°N and 16.02° E.



Figure 11 : The Saura MF radar

The key feature of this radar is its antenna system, the antenna array consists of a total of 31 antennas, of which typically 29 antennas are used for transmission and the remaining two antennas are to complement the receiving capabilities, these two antennas are used for the interferometric analysis of the detected signal. The 29 crossed half-wave dipoles arranged in the shape of a cross, called mills cross structure. The distance between the cross dipole is 0.7 radar wavelength. The beam width is  $6^\circ$  and thus results in a sufficiently small observation volume. A schematic of Saura MF radar is shown in Figure: 13 with its major component and antenna array. Each dipole is fed by its own transmitter / receiver unit with a power of 2 kW (phase-controlled for transmission and reception). This achieves a high level of flexibility in beam shaping and alignment. It is also possible to carry out measurements in right and left circular polarization matching with both magneto ionic components, the ordinary and extra ordinary components (o- and x-mode) for differential absorption and phase measurements. In addition, the antenna beam can be directed in the five directions NW, NE, SE, and SW at zenith angles. Furthermore, radar beams with different widths can be generated with the same swivel angle. The experiment conducted by Saura radar have a length of typically 220s and a pulse repetition frequency for daytime of 12 min long and consist of a vertical only experiment, five beam scanning experiment and a long range monitoring experiment. [7]

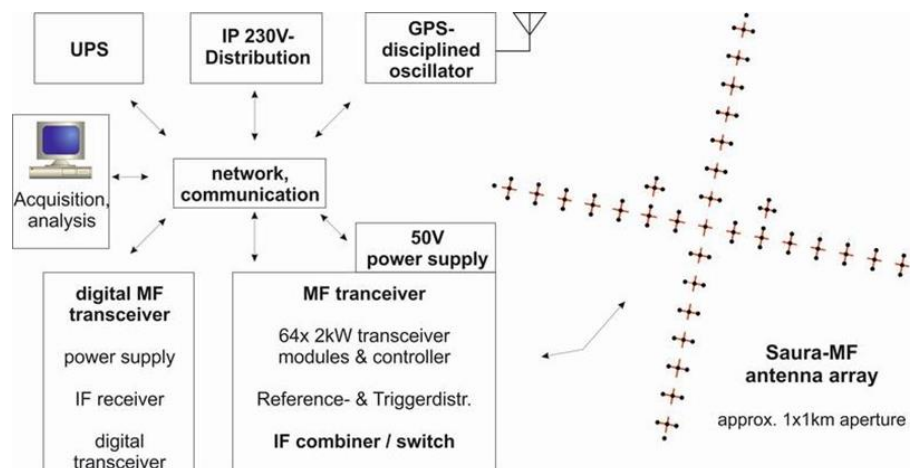


**Figure 12 :** Schematic structure of the Saura MF radar. [13]

## 2.2 Advantages of Saura MF radar

This radar is placed in polar latitude and hence it is very sensitive to enhanced ionization caused by solar and geomagnetic activity. It has very low frequency fluctuations, so even small electron number densities are sufficient to allow partial reflection from the sparsely ionized middle atmosphere. The coverage depends on the ionization state of the atmosphere and gets the best results from 50 km altitude and upwards. Other than wind observation, the Saura MF radar can be used to derive the turbulence parameters from the spectral width of the radar echoes. Furthermore, from the calibrated echo power, information about the atmospheric turbulence can be derived. The Saura radar is used with an exceptionally large antenna array and can be used for many atmospheric radar measurements. For example, Doppler beam swinging measurement, which is used for the estimation of wind and the electron density. The estimated electron density will give information about the ionization state of the middle atmosphere. For this, the differential phase and differential amplitude experiment (DPE, DAE) are utilized, by analyzing the relation of the ordinary and extraordinary mode for a given time and altitude. The experiments have a length of typically 220s and a pulse repetition frequency (PRF) for daytime of 100Hz. The entire measurement sequence consists of five beam scanning experiments and a long range monitoring experiment.

Geographic position	69.14°N, 16.02° E
Peak power	116kW
Range resolution	1000m
Antenna array	29+2 crossed dipole
Gain	17 dB
Beam width	6.4°
Number of receivers	9
Polarization	Circular, O/X
Beam positions	Typically 1 vertical and 4 tilted
Objectives	Estimation of wind, electron density

**Table 1:** Technical parameters of Saura MF. [13]

### 3 Particle precipitation events

#### 3.1 Overview

Due to solar activities, energetic particles precipitate into the atmosphere. These energetic particles include charged protons, electrons, galactic cosmic rays (GCRs) etc. These energetic particles entering the earth are guided by the interplanetary magnetic field (IMF) through space. The highly energetic electrons that are trapped in the van Allen belts and protons are penetrated to the earth during solar flare, while the GCRs are deflected by the IMF because of the strong activities of sun. The input of GCRs to the atmosphere are more, when the solar activities are low and these energetic particles ionize the atmosphere. The typical energies of EPP particles range from 1 MeV to few hundred MeV for proton, and from tens of keV to a few MeV for electrons. These particles with high kinetic energy enter at the polar cap regions and react with chemical species in the atmosphere, which leads to ionization of the atmosphere and thereby increases the production of HO<sub>x</sub> and NO<sub>x</sub>. These reactive nitric oxides and hydrogen oxide gases cause ozone (O<sub>3</sub>) depletion in the middle atmosphere. The energetic particle precipitation can also affect the temperature and dynamics of the atmosphere. The combined effect of SPEs and EPP results in stratospheric warming events and cooling rates, the mean circulation, wave propagation and breaking. Furthermore, NO<sub>x</sub> is one of the main participants in catalytic ozone destruction, [M. Sinnhuber et al. 2012]. The ozone loss in the middle stratosphere of up to 40% to 60% has been inferred from the correlation of observed EPP-NO<sub>x</sub> enhancements Randall [1998].

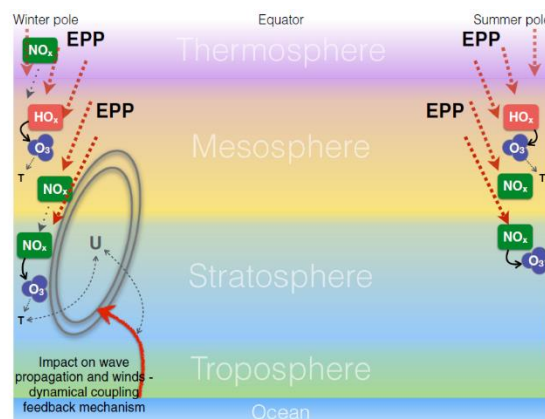


**Figure 13 :** Energetic particle precipitation (EPP). [15]

Figure 13, shows the main direct and indirect impacts from EPP (including EEP and SPE). EPP ionization is focused on the Polar Regions leading to the production of HOx and NOx. Transport processes are shown with grey dotted lines, while coupling mechanisms are indicated with grey dashed lines. Direct chemical impacts are shown with black arrows.

Additionally, Magnetospheric substorms reacts with geomagnetic field causes EPP and the enhanced ionization results in an ozone loss of 5-50% in the mesospheric region depending upon the seasons, [A. Seppälä et.al.2015]. Substorms provide a significant proportion of precipitating electrons. The Substorms consist of growth, expansion and recovery phase. The energy that is accumulated in the magnetosphere in the growth phase is released during the expansion phase. During expansion phase the magnetosphere return to a dipolar state and this changing magnetic field accelerates electrons and ions.

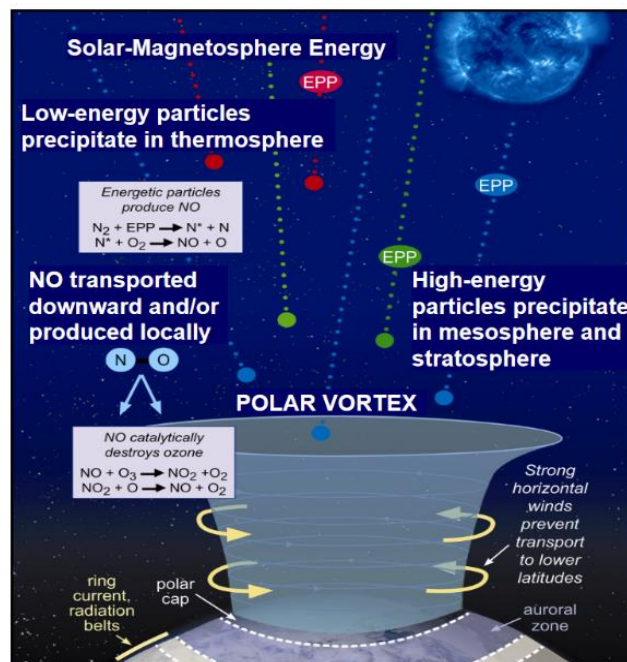


**Figure 14** : Energetic particle precipitation (EPP) impact on the atmosphere. [17]

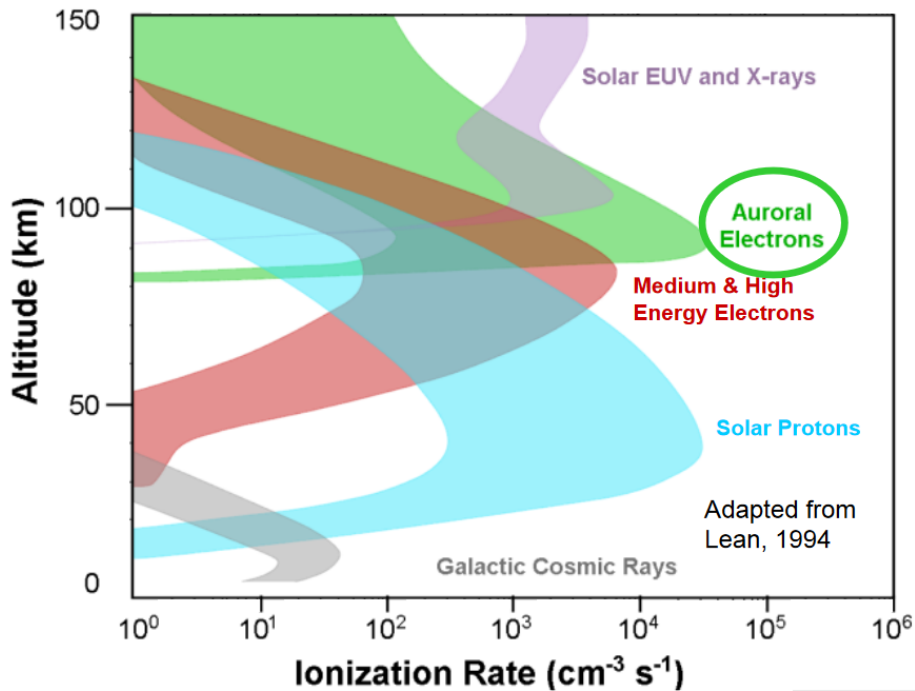


Figure 15: Ionization rate of EPP [17]

Unlike proton precipitation from SPEs, the electron precipitation does not take place homogeneously across the polar cap, but it is tied to the geomagnetic latitude around the auroral oval and the radiation belts. The ionization rates of solar proton events are very high compared to the others (Figure 15). The precipitation of the lower energy particles (<10 MeV), which occurs more frequently than the solar proton events are focused in this study.

### 3.2 Observation of particle precipitation events by Saura MF

Precipitation of the energetic particles increases the ionization in the atmosphere and it results in the rapid increase of electron number density in the ionosphere. The particles from various sources (from the aurora and the radiation belts during geomagnetic storms and substorms or from outside the solar system) have different energy spectra and interact differently with the terrestrial magnetic field. Therefore, they affect different altitudes in ionospheric region thereby varying the electron density. The detected echoes of the radar depends on absolute electron number density. The electromagnetic wave from the radar gets absorbed because of the energetic particles, so their amplitude decreases while propagating through the ionized plasma and sometimes vanishes.

The analysis was done using the pre analyzed DBS data by programming in python. The data from the beginning of 2017 to the end of 2020 is taken. The below flow chart (Figure17) will help to understand the algorithm used for the analysis.

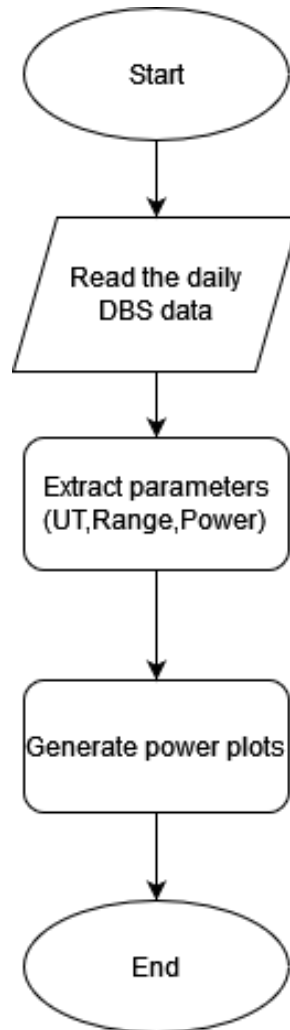


**Figure 16:** Flow chart for generating daily power plots.

The daily DBS data includes the received echo power, time (UT), the range in km from which the echo is reflected. Using these informations daily power plots were generated with range over time.

### 3.2.1 Analysis of Quiet and disturbed days

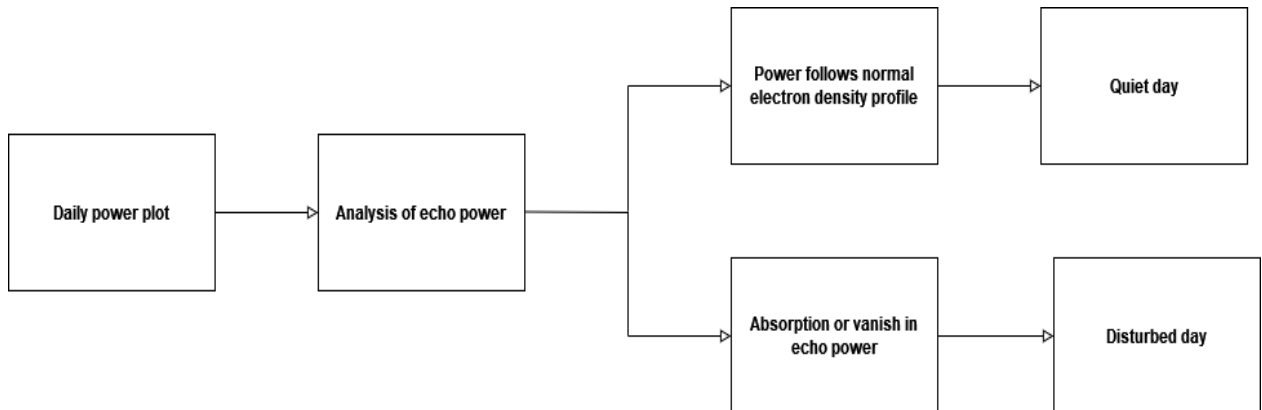


**Figure 17:** Block diagram of the analysis procedure.

As mentioned earlier, the normal electron density profile of D region is from 60 km altitude increasing towards 90km altitude. Generally, the days can be classified into two categories depending on the partial reflections observed with MF radar. Quiet days are days in which the partial reflection follow the electron density profile of D region. Whereas in disturbed days, severe ionization causes drastic reduction in echo power in the upper altitude, especially above 75km altitude.

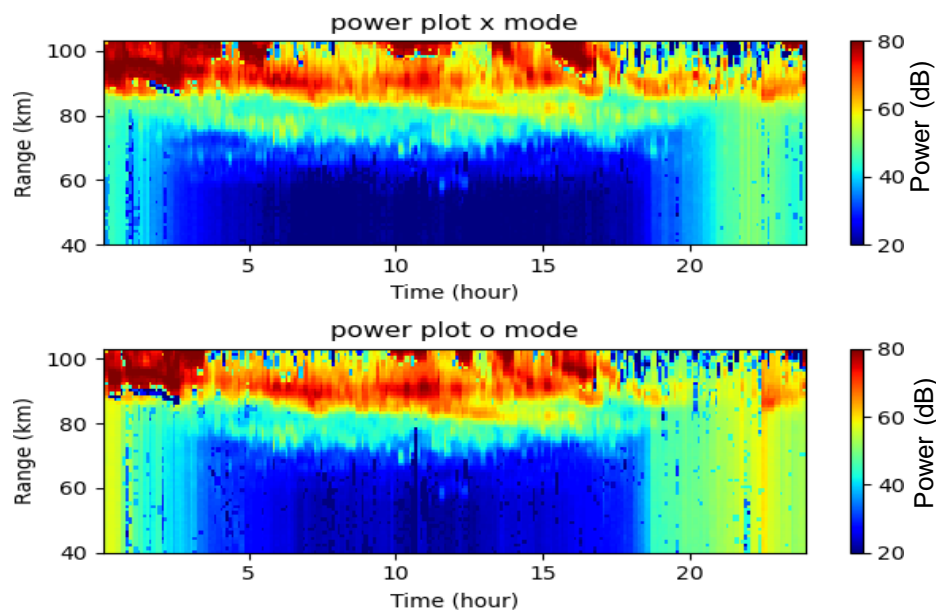


**Figure 18:** Power plot of a quiet day.

In the example (Figure 18) of power plot for a quiet day, first echoes are seen around 60 km altitude and it increases gradually towards the higher altitude. In this the echo intensity roughly follows the electron density profile of D region. On the contrary, in disturbed days solar and geomagnetic conditions varies and as a result of this ionization shoots up and due to the increased ionization of highly energetic particles the emitted electromagnetic waves gets progressively absorbed. As a result of this particle precipitation events, ionization will increase and so echoes from lower altitudes are seen. So the maximum echo power is visible at these altitude and at higher altitude high absorption is observed. Furthermore, a thin layer is formed at lower altitude.

These absorption is commonly seen in the forenoon times (9:00 to 13:00 UT). Compared to the ordinary mode intensity the extraordinary mode gets attenuated more. The example for a disturbed day is indicated in Figure 19, in this x mode component gets absorbed more from 5 to 10 UT and apparent layer is visible at 60km altitude. These layers are termed as isolated lower mesospheric echoes (ILME) [C: M: Hall et.al.2006]. For some days, due to high ionization layers are seen even below this altitude, which will be explained later.

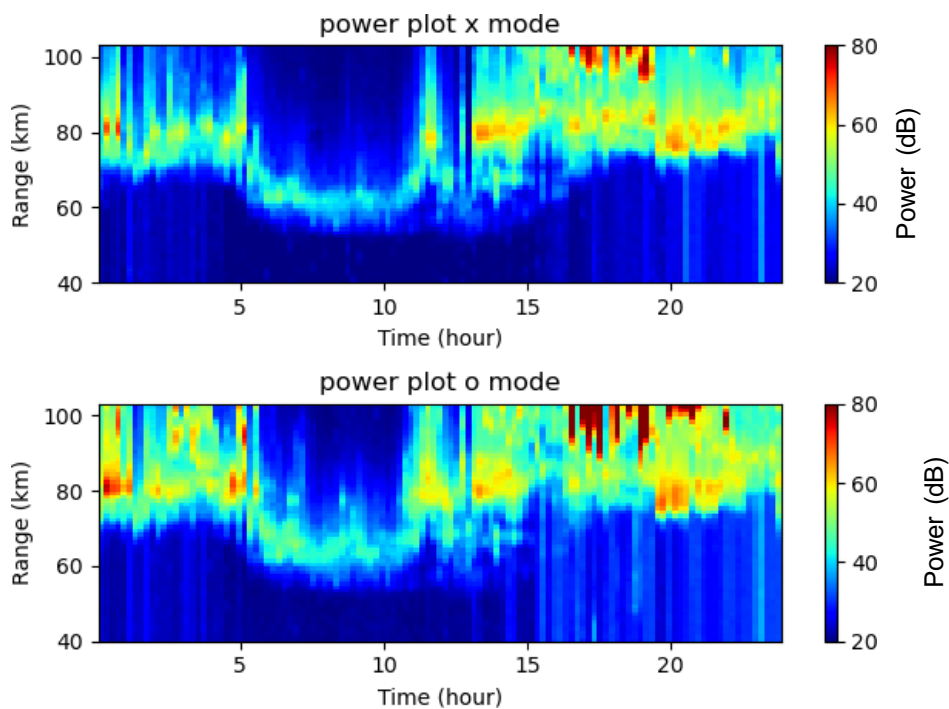
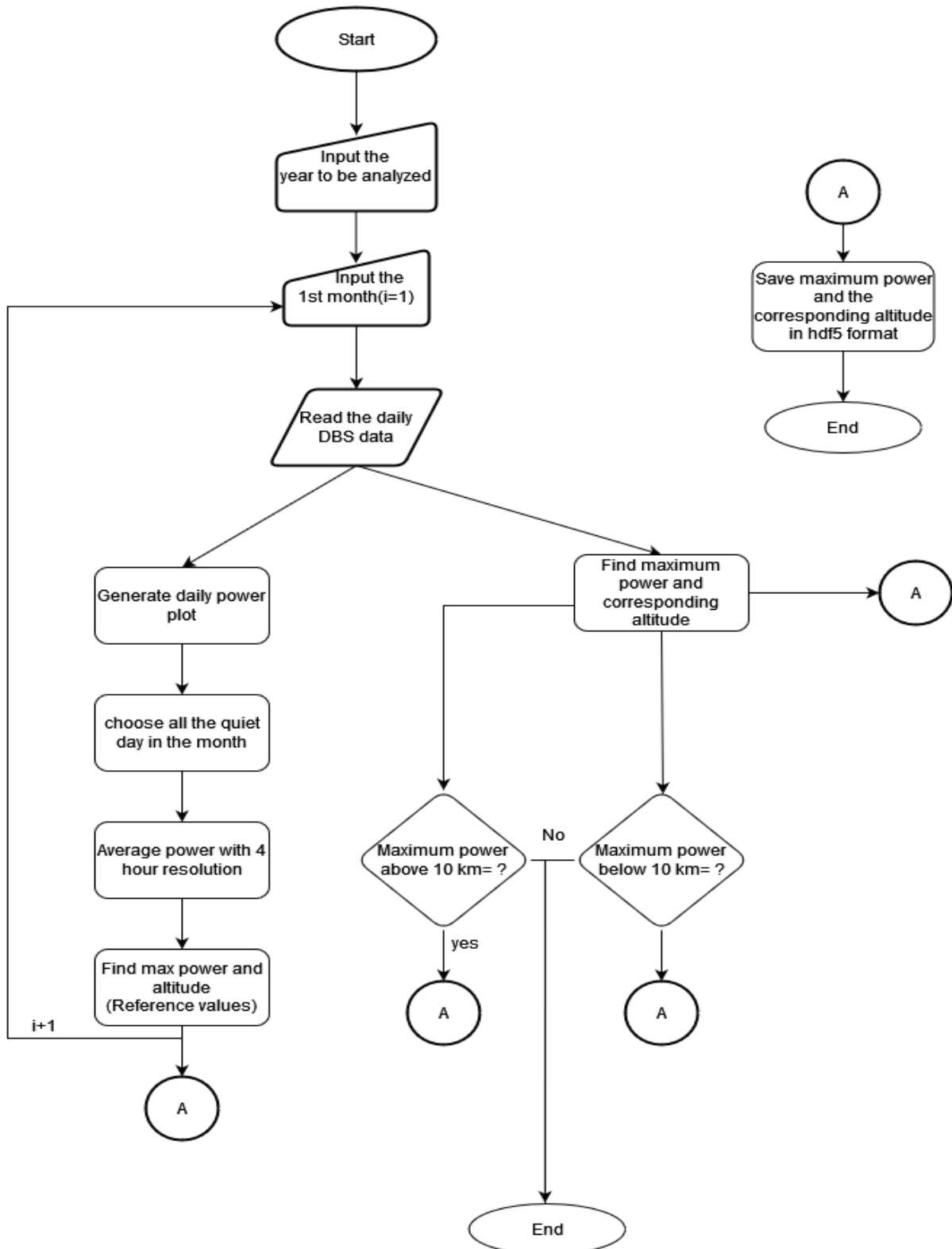
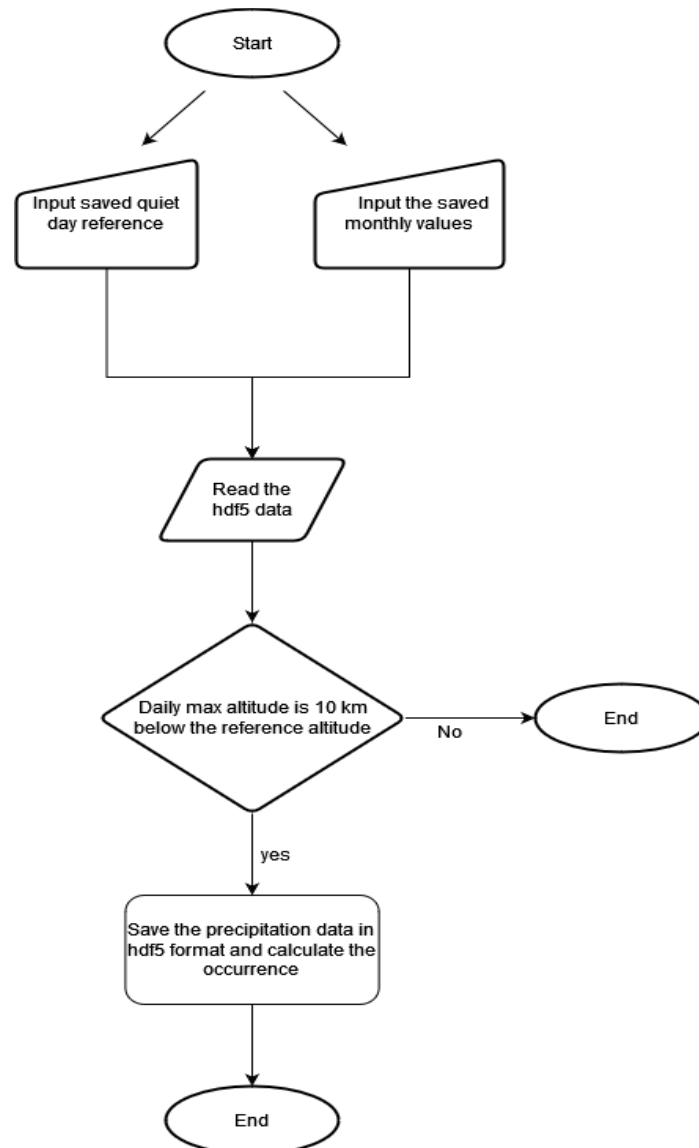


Figure 19: Power plot of a disturbed day.

### 3.3 Selection of ILME events from DBS data

The dataset which is used for daily power plot analysis is again used for the analysis of ILME events formed due to particle precipitation.





**Figure 20:** Flow charts for calculating the ILME events.

The flowchart 20 explains how the events are selected. All the quiet days in a month shows somewhat a same behavior and so these days were averaged to get a monthly quiet day reference profile. The reference profile for all the months are generated by averaging the observed individual profiles. The maximum power and altitude corresponding to the maximum power is obtained from the derived average power and these datas are stored as an hdf5 format. These datas are considered to be the reference power and reference altitude (normally found in between 75-90 km) for doing the further analysis. The quiet day reference profile obtained for the month of February 2018 in shown in the figure 21.

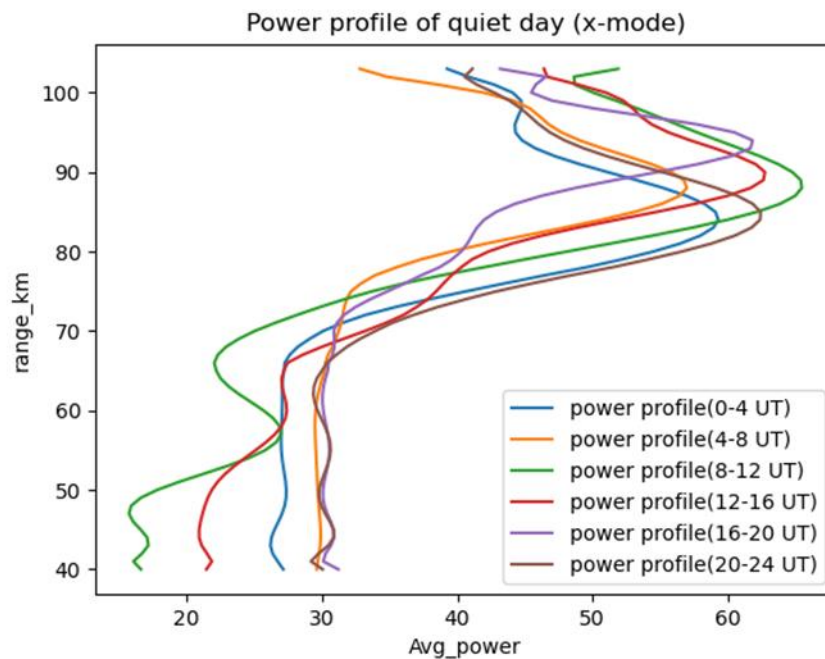


**Figure 21:** Monthly power profile for quiet days.

During late night and early morning, strong interference occur from other distant transmitters. In this 4 hours resolution, it is clear that during day time when the availability of sun is more gives maximum power and during other times of a day the average power obtained is less compared to the 8 -12 UT and the disturbances are observed mostly in the lower altitude regions. In this quiet day profile the maximum power is observed around 88 km altitude.

Similarly, the peak power and the altitude corresponding to all individual days spanning a period of 4 years are obtained. For making the analysis more reliable, the power profile are smoothed by using Savitzky Golay filter. Sometimes, maximum powers (second maximum) were observed above or below the observed maximum power. So I checked whether there is any maximum power available in 10 km above and below the observed maximum power and the corresponding altitude for all the cases are saved as an hdf5 format. After this, the peak values obtained is compared with the quiet day reference values, which is already saved.

The comparison of the maximum power values of the day under investigation to the quiet day reference gives the precipitation events. In Python, a yearly precipitation event vector is generated and for making this vector, I have applied a condition. If the maximum power obtained on an investigated day is 10 km below the reference value of the quiet day, then it is occurred due to particle precipitation. By applying this condition, one can clearly differentiate a disturbed day from a normal day. So that the disturbed days can be easily differentiated from the normal days. The difference of these layers from reference height gives a clear idea about the intensity of the particle precipitation events. After obtaining the precipitation vector for all the four years, the plots are made.

### 3.4 Statistics of Particle precipitation occurrence

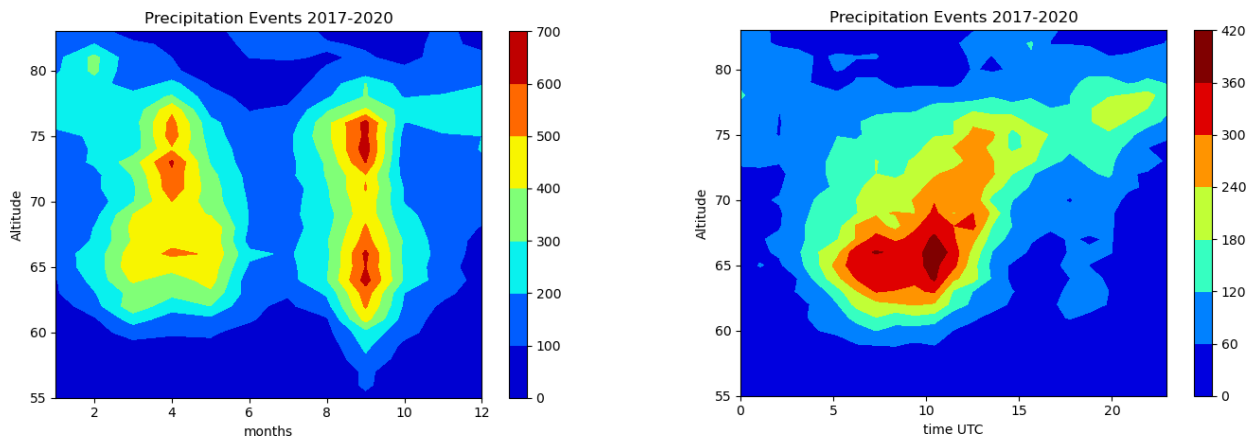


**Figure 22:** Annual occurrence of ILME events (Absolute counts) form 2017 to 2020.

In this section, the statistics of the detected particle precipitation into the mesosphere are presented and discussed. During March- April and August – October and from 6:00 – 12:00 UT, precipitation events are observed most frequently (Figure 22). In the combination of particle precipitation detections from the year 2017 to 2020, the ILME events are more prevalent in spring and autumn. Additionally, the counts are seen around 63km altitude and at 10 UT. Less number of counts were seen down to 55km

altitude. Taking individual years in to account, the behavior was almost same except in 2017, which will be discussed later. The maximum occurrence rate from the year 2018 to 2020 was found to be around 35- 40%.

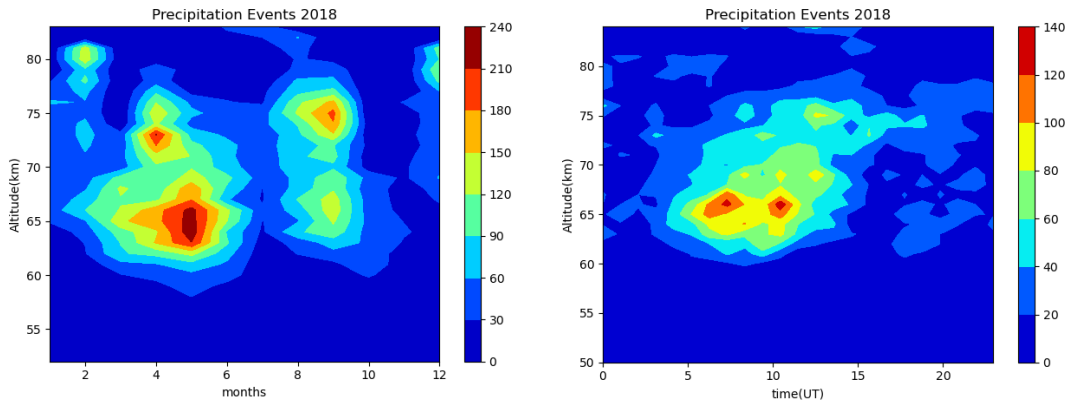


**Figure 23** : Particle precipitation events obtained for 2018.

The particle precipitation events of the year 2018 show an occurrence rate of 36% in September, which was the highest and 31% in March. In all the other years the count rate was around 40% in both the times. On the whole, the highest count rates were observed in spring and autumn equinoxes as explained earlier. In these three years, a higher number of precipitation events occurred on March- April than in August-September. The events were been observed mostly around 65 km altitude and at the same time less number of events were observed down to 52km altitude. Furthermore, most events were visible around the magnetic noon. Events were also visible in night times, however with less count rates. The interference of distant transmitters were also seen in night times. During the times of ILME occurrence, these interference are not present because of the intense absorption.

### 3.4.1 Special Case

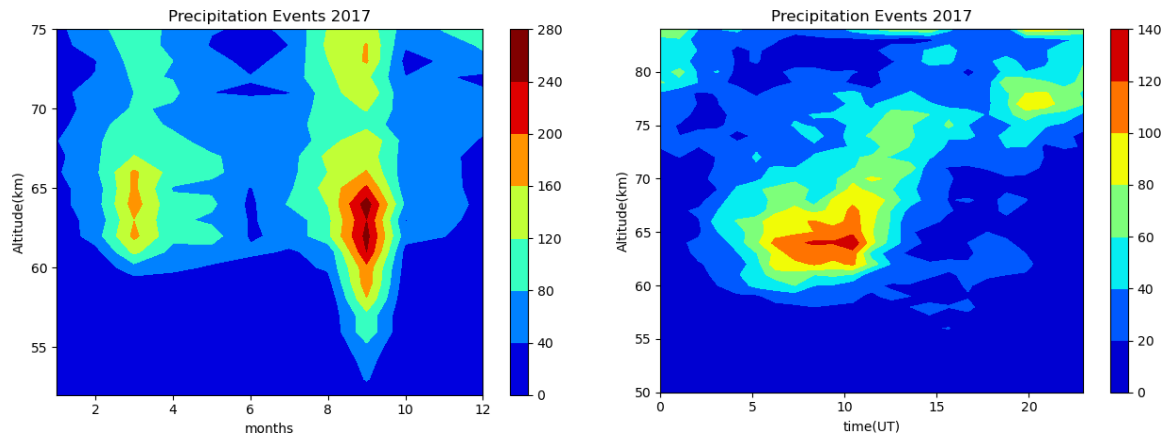


**Figure 24** : ILME events in 2017.

2017 was a special year, in this year very high number of particle precipitation events was observed. As explained, one of the reasons for the occurrence of precipitation events are geomagnetic storm. The month of September in this year was an exceptional case as there was intense solar activities. From 6-10<sup>th</sup> September, the sun emitted twenty seven M class and four X class flares and released several coronal mass ejections [Lina Tran, 2017].

CME are capable to generate powerful geomagnetic storms in Earth's magnetic field. On 7<sup>th</sup> and 8<sup>th</sup> September severe and multiple geomagnetic storming were observed, AGU [2021]. In short, high ionization happened and results in very high number of precipitation events due to this active geomagnetic storms. The occurrence rate in September was very high when compared with the occurrence in spring season. This remarkable increase can be seen in the plot also (Figure 24). The ILME events down to 52km altitude can be seen clearly in this plot.

### 3.5 Comparison of the observations with previous analysis.

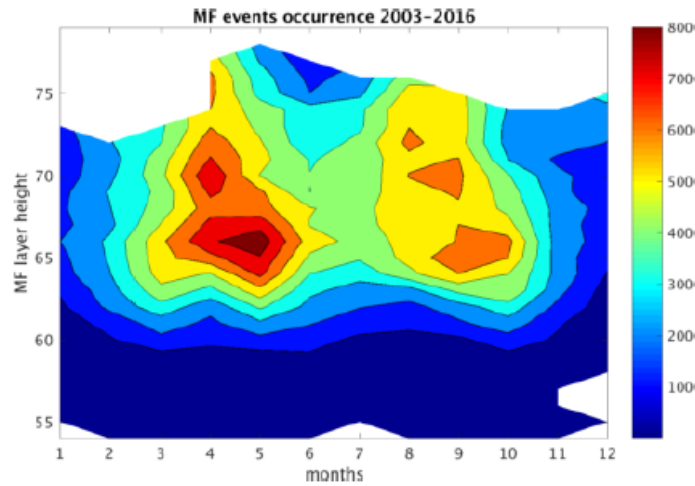


**Figure 25** : Annual particle precipitation events obtained from the year 2003 to 2016. [9]

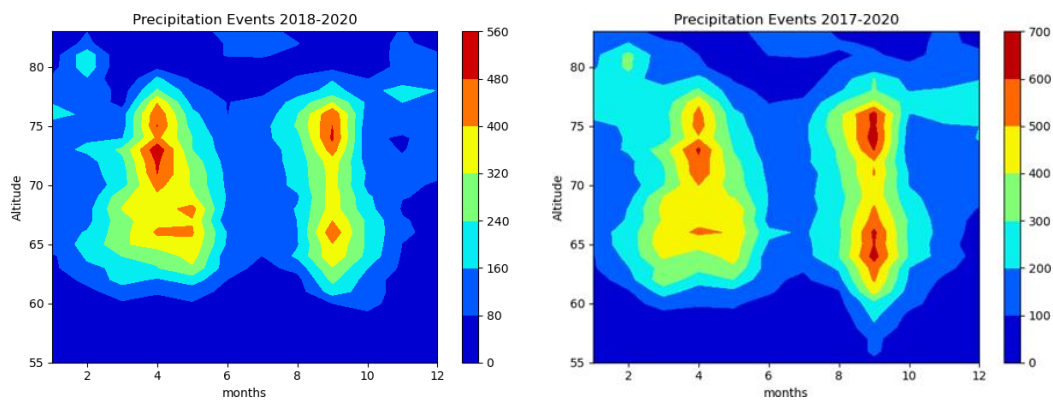


**Figure 26** : Observed ILME events (Absolute counts) in the current study.

Comparing the observations done by T. Renkwitz and R. Latteck [2017] (Figure 25) for the period ranging from 2003 to 2016 with my observations in the period 2018 to 2020 (figure 27), one can say that precipitation events in spring season is higher than in autumn season. I have got a similar pattern of annual occurrence plot like in the study of Renkwitz and Latteck expect for the year 2017(Figure 26 left panel). However, if 2017 is included then due to higher number ILME events because of geomagnetic storms, the plots shows a contrary results to the previous observations.

### 3.5.1 Geomagnetic indices

Geomagnetic indices plays a key role in characterizing the state of the entire Earth's magnetosphere as well as that of the surrounding interplanetary medium (IMF). These are used for detecting and describing atmospheric events. Geomagnetic events measures the geomagnetic activities which is a signature of the response of the Earth magnetosphere and ionosphere to solar forcing [Menvielle et.al. 2011]. The indices which measures the geomagnetic activities are K and A index, they give indications of the severity of magnetic fluctuations and hence the level of disturbance to the ionosphere. The K index, which is measured using magnetometer is a three hourly measurement of the variation of the Earth's magnetic files compared to quiet day conditions. It defines the disturbances (geomagnetic storms) in the horizontal component of earth's magnetic field, representing calm to greatly disturbed conditions with integer range from 0-9. The A index is a linear measure of Earth's filed and is derived from K index. Ap and Kp indices are the planetary average of all the A and K indices.

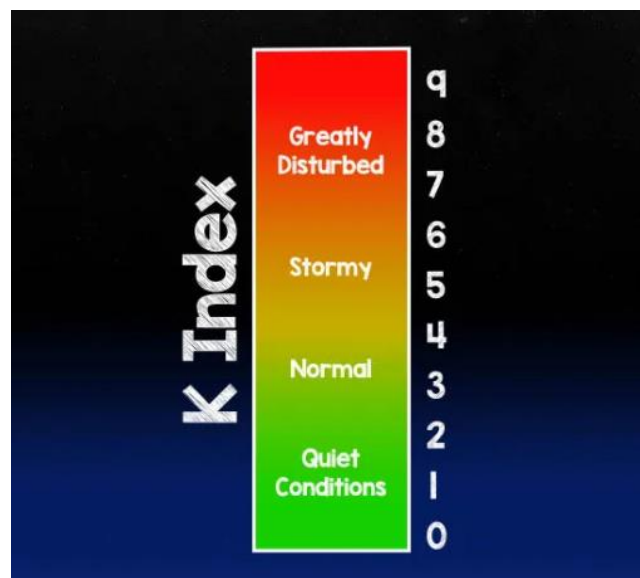


**Figure 27:** Relation between the Kp index and ionospheric conditions. [22]

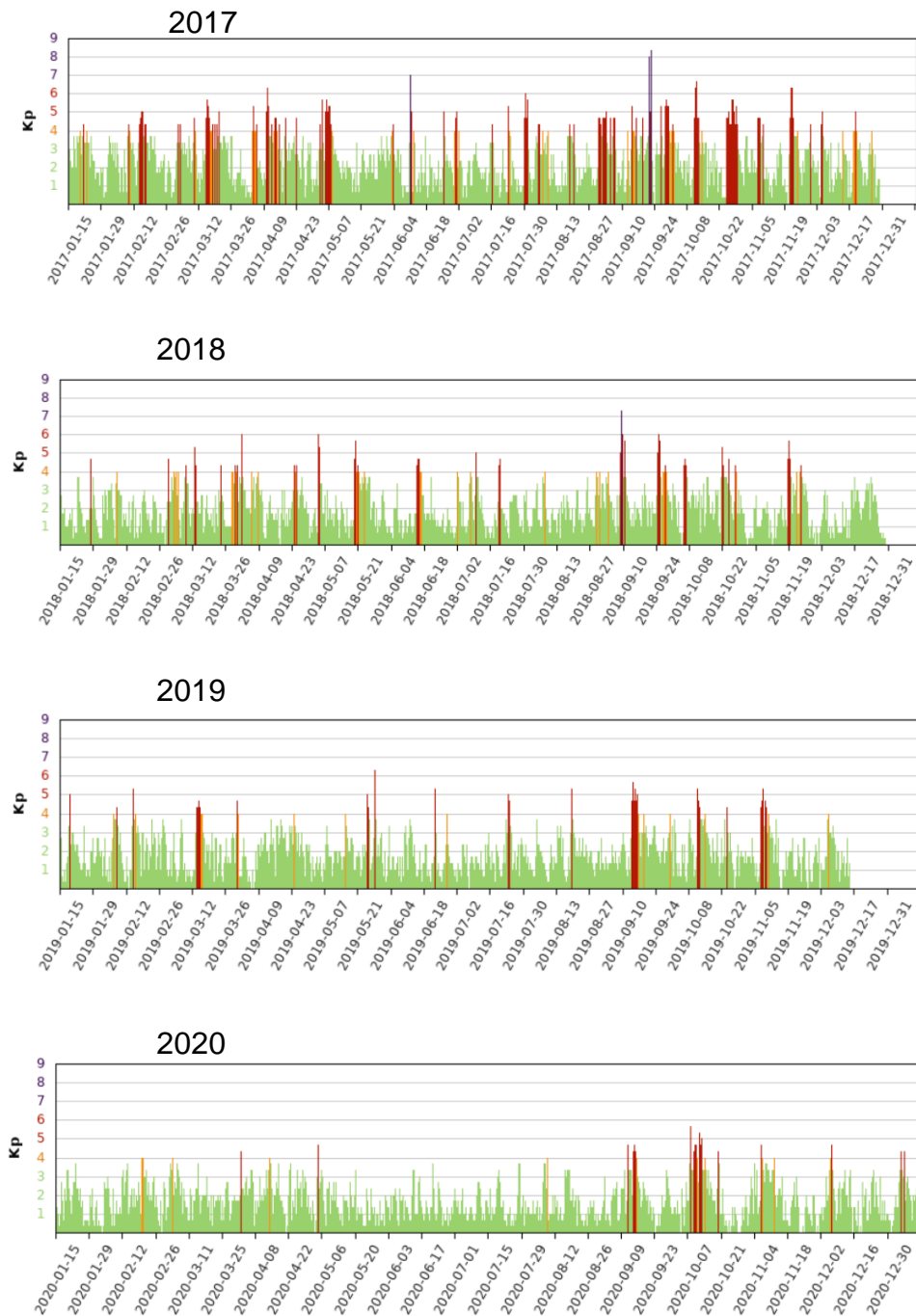
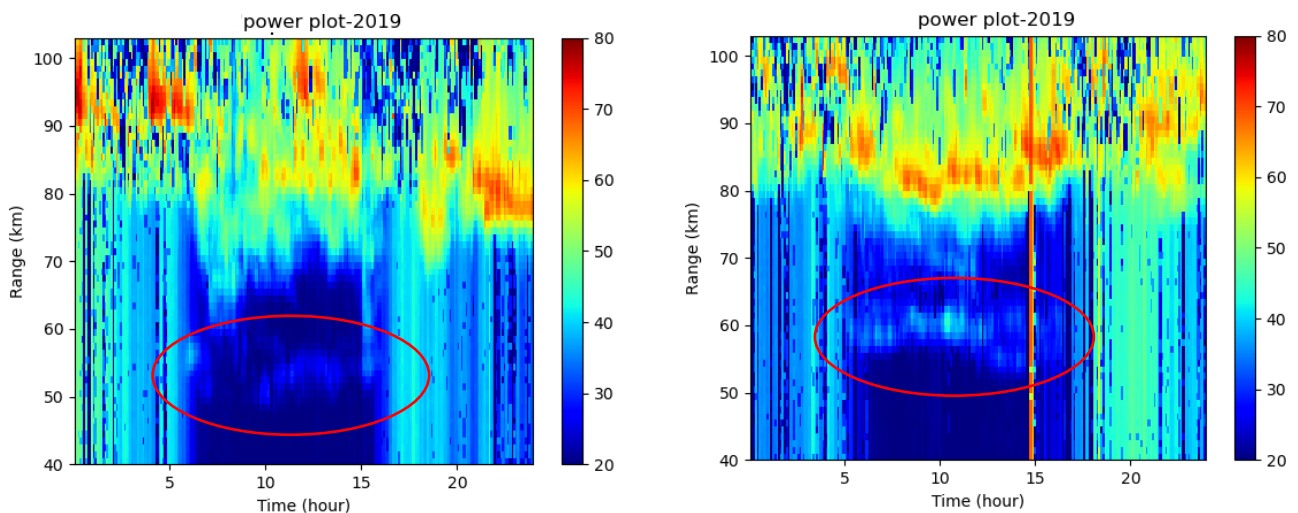


Figure 28 : The Kp index from the year 2017 to 2020.

Highest number of Kp index in 2017, results in large precipitation events. The plot was generated using NMDB online data access tool. [23]

#### 4 Investigation of ionospheric layers by analyzing radar raw data

In the previous section, the ILME occurrence due to particle precipitation events were analyzed by using the DBS data. Here the layers due to particle precipitation and also layer occurring without much visible particle precipitation are analyzed using the original radar raw data. The days in which layers are formed due to particle precipitations were very clear, because from the daily plot analysis the disturbed day can be easily analyzed and so the particle precipitation events and the layer occurrence is well understood. There were days having no visible indication of particle precipitation or even without precipitation. However, a layer is persistent throughout the day or sometimes during the noon time, which shows that there may be layers occurring at lower altitude of the ionosphere without the precipitation events.



**Figure 29:** Layer present at lower altitude (red circles) seen in the power plots of x-mode for 14<sup>th</sup> and 21<sup>st</sup> March 2019

The power plots (Figure 29) depicts the presence of an isolated layer between 50 and 65 km altitude without visible particle precipitation events (At higher altitude there is no much absorption of echo power). The layer is seen mainly in day time and high level of interference is observed during early morning and night times. Due to these interference, the layers are not visible at these times in the daily power plots. The days having isolated layers were specially analyzed by using the radar raw data by calculating the spectrum.

Ideally the radar echo of an antenna is assumed to be like a pencil beam, but in actual case the radiation pattern may have side lobes [R. Latteck and T.renkwitz, 2019], because of the presence of turbulent cells or for multiple atmospheric scatters, which may result in broadening of the spectra. Sometimes the highly efficient scatters are away from the vertical or the nominal beam pointing direction, but in the side lobe position. These are still within the view of the radar and such situations leads to super position of the oblique scatter with the vertical echo. Actually, the oblique echoes for the same altitude have a different range but it is smeared into higher vertical amplitude. To avoid or to overcome these situations interferometric methods are used to estimate the scattering position of the individual echoes.

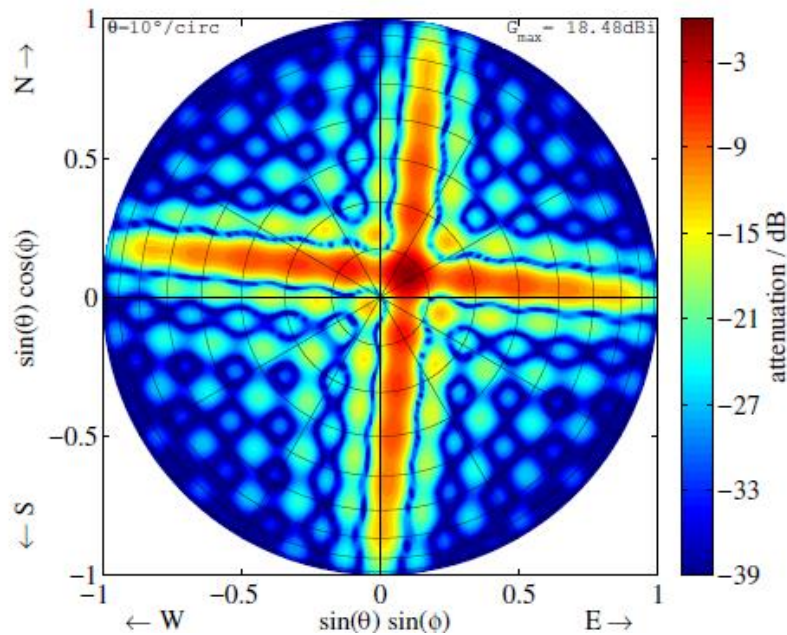


**Figure 30:** Simulated radiation pattern of the Saura MF radar pointing to  $\phi=56.2^\circ$  and  $\phi=6.8^\circ$ . The narrow main lobe as well as pronounced side lobes are visible.

[24]

4.1 Analysis procedure

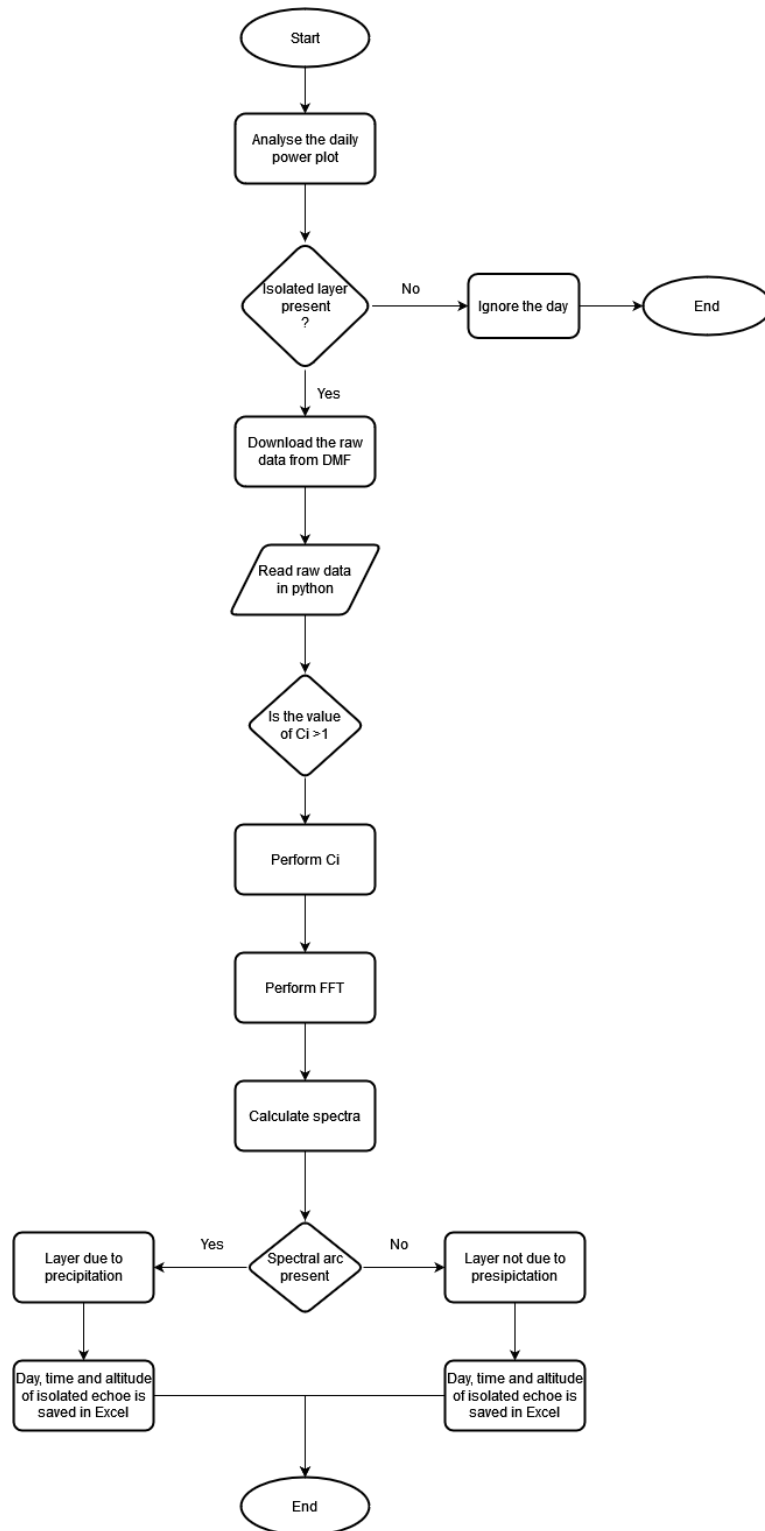


Figure 31: Flow chart for the analysis of isolated layers by raw data.

The flow chart (Figure 31) shows the detailed analysis of the layer by using raw data. For this, the daily power plots were analyzed and separated the days with and without isolated layers. The days without layers were no longer considered for further analysis and the days with isolated layers are considered and the radar raw data for the corresponding days has been downloaded from DMF. The DMF data of Saura MF for the particular month and year was chosen and then by using the command 'dmget', retrieved the radar raw data of a particular day from the vertical experiment or sometimes the sd-07-ox4c experiment. The generated daily spectra from the original radar raw data were analyzed. The calculation of the spectra and the inferences will be discussed in the coming sections.

### 4.1.1 Data migration facility (DMF)

DMF is a software used to transfer files mainly with the purpose to allow users to keep an increased volume of data in the files under their home directories. Radar raw data need a very large amount of space and hence in this application DMF plays an important role.

This software transport large volume of data from a high performance device to a low performance device, which is commonly called a secondary storage. DMF is able to transfer or recall the transferred data. It keeps the disk space available to user by moving unused files to storage on tape.

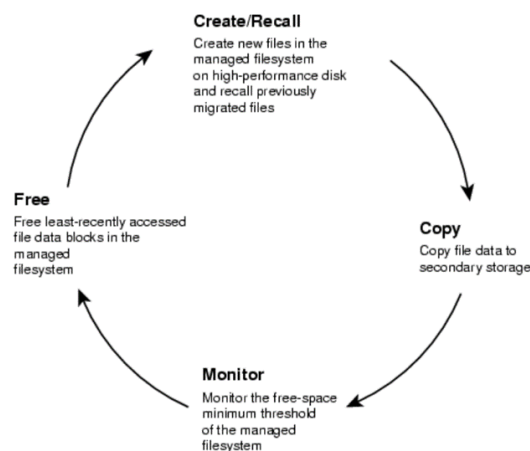


**Figure 32:** DMF migration cycle between the managed file system and the secondary storage. [38]

The DMF commands list, put, find and get files of tape are used for controlling the file transfer for example, if we want to retrieve the migrated files to active disk for the purpose of read or write we normally use these DMF commands (Table 2).

Commands	Description
dmls	Directory listing showing file migration status
dmget	Retrieve migrated files to disk
dmput	Cause files to migrate to backup on tape
dmfind	Find files under a directory hierarchy
dmcopy	Copy all or part of offline files
dmattr	List attribute of files

**Table 2:** Commands used for operating DMF system. [38]

The managed file system (XFS or CXFS) is mounted with an enabled Data Management Application Programming Interface (DMAPI) on the high performance disk and it is always monitored by the DMF software, so that it can maintain a certain amount of free space in the file system, which allows creation of new files or recalls the migrated one. If the free space threshold exceeds then the DMF transports the data files. For this, the data is first copied to a secondary storage and then data blocks is released by monitoring the access time and its size. It always keeps the timely data on the high performance disk and shifts the other to secondary storage by keeping a files metadata. In order to prevent the file data loss like, failures in the storage device or deletion of migrated copy occurs, it won't affect the DMF environment because it creates two secondary storage copies of the files. However, the users is able to access all the files regardless of the time or actual location of the data. DMF software can migrate data to different media like Disk, Fiber channel tapes and tape libraries that are supported by the Open Vault or TMF mounting services, Cloud storage, and another servers via FTP etc. DMF is a very cost effective method for transferring infinite amount of data without sacrificing accessibility of users.

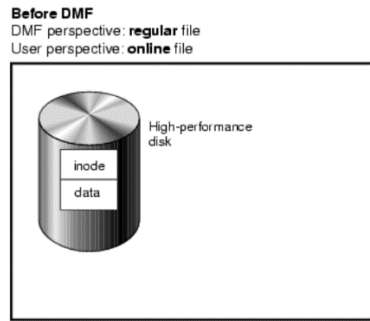


Figure 33: DMF before migrating data. [38]

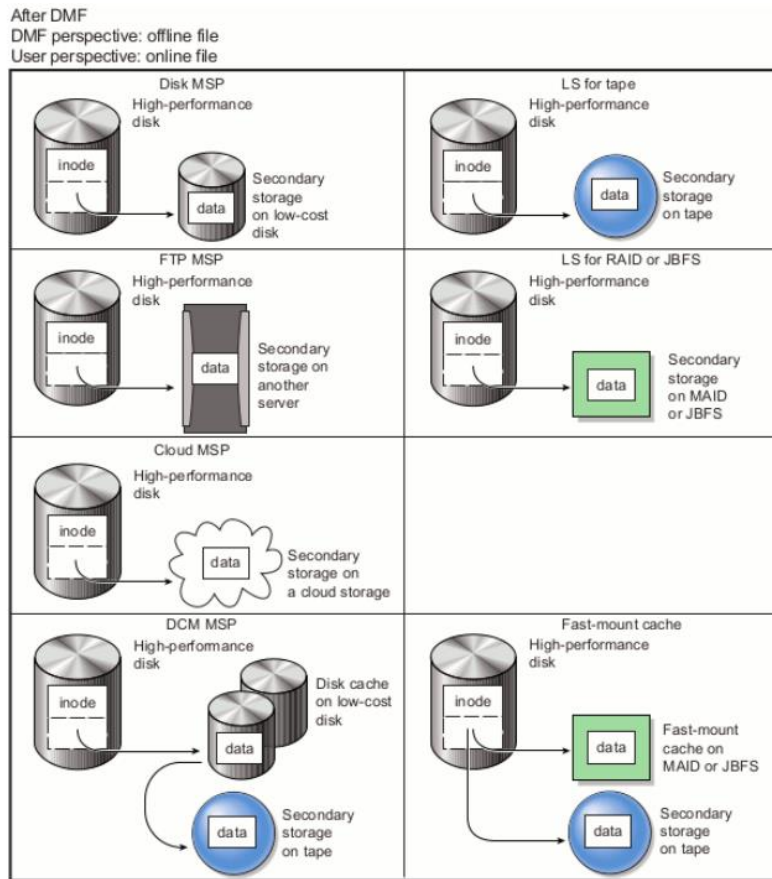


Figure 34: DMF after data migration and freeing space. [38]

## 4.2 Calculation of spectra using python

The programming language Python was used for the calculation and analysis of spectra. As mentioned in the previous section, the downloaded original radar raw data is used for programming. In python, the day (24 hour) having isolated layer was imported and from that, the raw o-mode and raw x-mode power of the hourly data is extracted. Thereafter a suitable number of coherent integration was applied to improve the signal to noise ratio. After that, I have converted the time domain signal to frequency domain by taking the FFT and then the spectrum is calculated and plotted the magnitude of the spectra. Then the analysis of the spectra was done for the purposes as follows:

1. For finding the days with and without precipitation.
2. For finding whether the isolated layers are subjected to particle precipitation or not.
3. For finding the time period of occurrence of isolated layer.
4. For finding the months having the highest occurrence rate of layers with and without precipitation in a year.

```

32 no_rangex=np.shape( rawx )[0]
33 no_rxtop=np.shape( rawx )[1]
34 no_sampx=np.shape( rawx )[2]
35 no_polndata=[['rx_polardata']]
36 no_cldata=[['raw_cld_spr']]
37
38
39
40
41 samples=np.linspace(1,np.shape( rawx )[2],np.shape( rawx )[2])
42
43 prfdata=[['prf']]
44
45 rangeinds=[['west_range_1'] / 1000
46 rangeinxrangelin = data[0][['range_xrangel_1'] / 1000
47 rangeinds=[['range_xrangel_1'] / 1000
48 rangex=np.linspace( rangeinxrangelin, rangeinxrangelin, int( (rangeinxrangelin) ) )
49
50 timevecdata=[['time_stamp_vec']]
51 t_start=(timevec[0]+timevec[1])*(60+timevec[2])/(60*60)/24
52 # t in unit (hour)
53 t=np.linspace( t_start, t_start+(1/prf)*(no_pol*no_cld)*no_samples/(60*60*24), no_samples, endpoint='True')
54
55 # t in hours
56 # t in hours
57 # t in hours
58 tsec=t*3600*60
59
60 # Res=17 -1
61
62
63
64
65
66
67
68
69
70
71
72
73
74
75
76
77
78
79
80
81
82
83
84
85
86
87
88
89
90
91
92
93
94
95
96
97
98
99
100
101
102
103
104
105
106
107
108
109
110
111
112
113
114
115
116
117
118
119
120
121
122
123
124
125
126
127
128
129
130
131
132
133
134
135
136
137
138
139
140
141
142
143
144
145
146
147
148
149
150
151
152
153
154
155
156
157
158
159
160
161
162
163
164
165
166
167
168
169
170
171
172
173
174
175
176
177
178
179
180
181
182
183
184
185
186
187
188
189
190
191
192
193
194
195
196
197
198
199
200
201
202
203
204
205
206
207
208
209
210
211
212
213
214
215
216
217
218
219
220
221
222
223
224
225
226
227
228
229
230
231
232
233
234
235
236
237
238
239
240
241
242
243
244
245
246
247
248
249
250
251
252
253
254
255
256
257
258
259
260
261
262
263
264
265
266
267
268
269
270
271
272
273
274
275
276
277
278
279
280
281
282
283
284
285
286
287
288
289
290
291
292
293
294
295
296
297
298
299
300
301
302
303
304
305
306
307
308
309
310
311
312
313
314
315
316
317
318
319
320
321
322
323
324
325
326
327
328
329
330
331
332
333
334
335
336
337
338
339
340
341
342
343
344
345
346
347
348
349
350
351
352
353
354
355
356
357
358
359
360
361
362
363
364
365
366
367
368
369
370
371
372
373
374
375
376
377
378
379
380
381
382
383
384
385
386
387
388
389
390
391
392
393
394
395
396
397
398
399
400
401
402
403
404
405
406
407
408
409
410
411
412
413
414
415
416
417
418
419
420
421
422
423
424
425
426
427
428
429
430
431
432
433
434
435
436
437
438
439
440
441
442
443
444
445
446
447
448
449
450
451
452
453
454
455
456
457
458
459
460
461
462
463
464
465
466
467
468
469
470
471
472
473
474
475
476
477
478
479
480
481
482
483
484
485
486
487
488
489
490
491
492
493
494
495
496
497
498
499
500
501
502
503
504
505
506
507
508
509
510
511
512
513
514
515
516
517
518
519
520
521
522
523
524
525
526
527
528
529
530
531
532
533
534
535
536
537
538
539
540
541
542
543
544
545
546
547
548
549
550
551
552
553
554
555
556
557
558
559
560
561
562
563
564
565
566
567
568
569
570
571
572
573
574
575
576
577
578
579
580
581
582
583
584
585
586
587
588
589
590
591
592
593
594
595
596
597
598
599
600
601
602
603
604
605
606
607
608
609
610
611
612
613
614
615
616
617
618
619
620
621
622
623
624
625
626
627
628
629
630
631
632
633
634
635
636
637
638
639
640
641
642
643
644
645
646
647
648
649
650
651
652
653
654
655
656
657
658
659
660
661
662
663
664
665
666
667
668
669
670
671
672
673
674
675
676
677
678
679
680
681
682
683
684
685
686
687
688
689
690
691
692
693
694
695
696
697
698
699
700
701
702
703
704
705
706
707
708
709
710
711
712
713
714
715
716
717
718
719
720
721
722
723
724
725
726
727
728
729
730
731
732
733
734
735
736
737
738
739
740
741
742
743
744
745
746
747
748
749
750
751
752
753
754
755
756
757
758
759
760
761
762
763
764
765
766
767
768
769
770
771
772
773
774
775
776
777
778
779
780
781
782
783
784
785
786
787
788
789
790
791
792
793
794
795
796
797
798
799
800
801
802
803
804
805
806
807
808
809
810
811
812
813
814
815
816
817
818
819
820
821
822
823
824
825
826
827
828
829
830
831
832
833
834
835
836
837
838
839
840
841
842
843
844
845
846
847
848
849
850
851
852
853
854
855
856
857
858
859
860
861
862
863
864
865
866
867
868
869
870
871
872
873
874
875
876
877
878
879
880
881
882
883
884
885
886
887
888
889
890
891
892
893
894
895
896
897
898
899
900
901
902
903
904
905
906
907
908
909
910
911
912
913
914
915
916
917
918
919
920
921
922
923
924
925
926
927
928
929
930
931
932
933
934
935
936
937
938
939
940
941
942
943
944
945
946
947
948
949
950
951
952
953
954
955
956
957
958
959
960
961
962
963
964
965
966
967
968
969
970
971
972
973
974
975
976
977
978
979
980
981
982
983
984
985
986
987
988
989
990
991
992
993
994
995
996
997
998
999
1000

```

Figure 35 : Spyder window

### 4.3 Preparation of the data set

This section describes how a data set is prepared from the spectral analysis. For this, raw data from 2017 to 2020 was taken and the spectra was calculated for the days having isolated layer in the daily power plots. In this the pattern of the spectra shows information about the particle precipitation. Due to particle precipitation events, the spectrum broadens to form an arc like shape. If the spectral arc is visible, it is considered to come under the category of time with precipitation and if echo is visible without this arcs, then it comes under the category of time without particle precipitation. The radar is conducting 15 experiments per hour including five vertical experiments for getting the raw data. In this analysis the raw data (several terabytes) taken is mostly from vertical experiments.

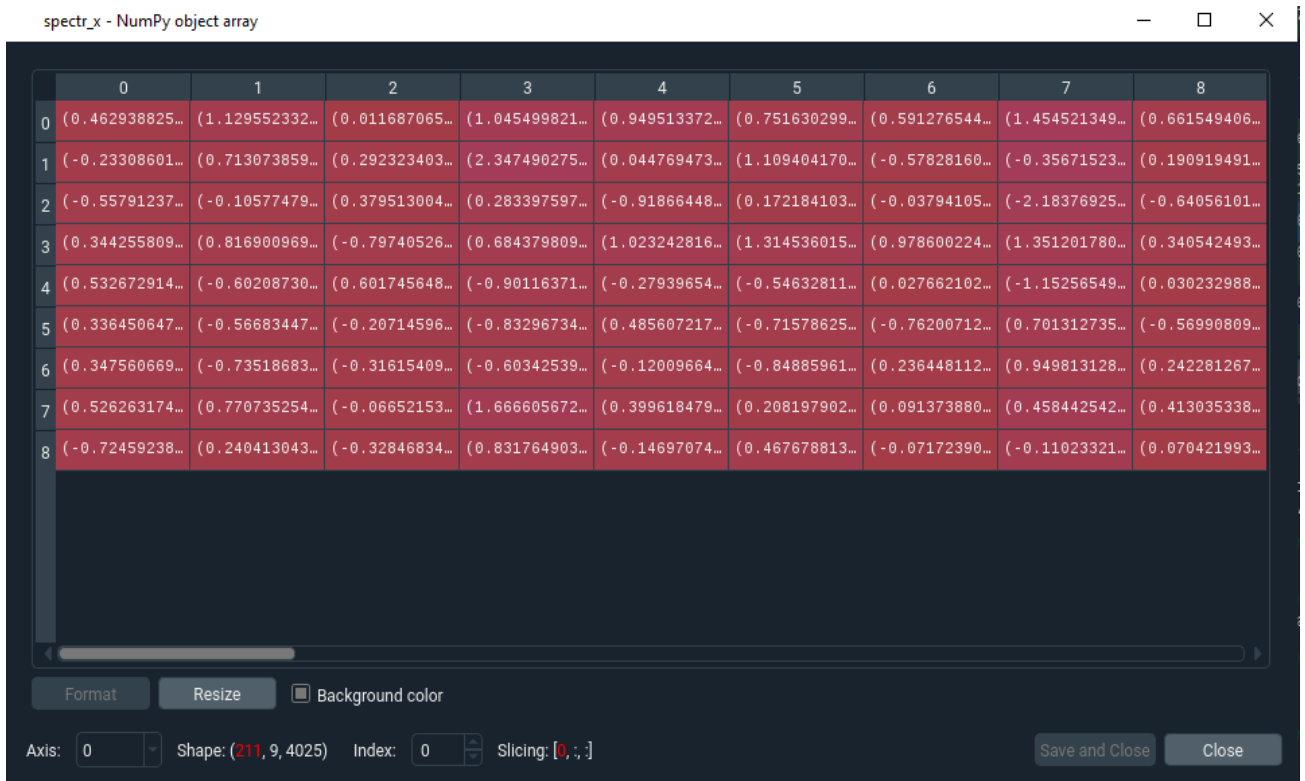


Figure 36 : Raw data block of x-mode power for 2018/03/01 at 4:04 UT

## 4 Investigation of ionospheric layers by analyzing raw data

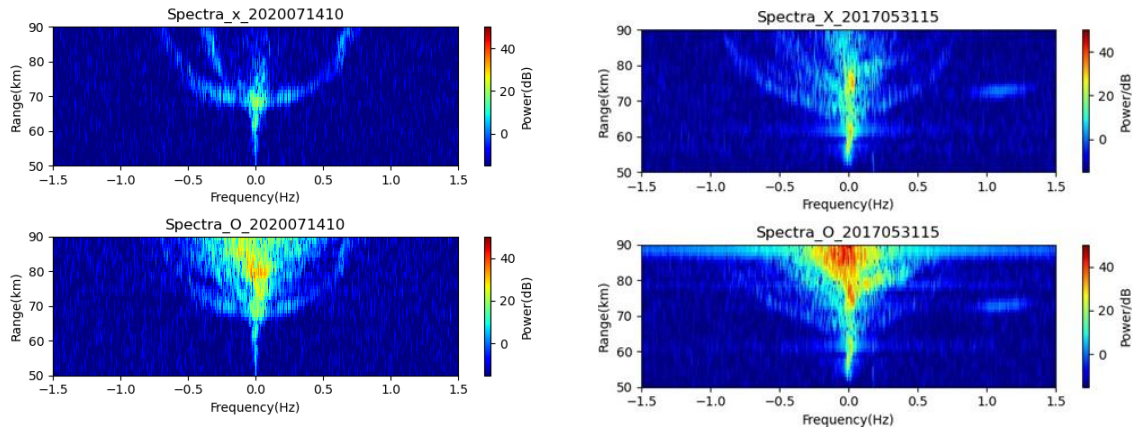


Figure 37 : Spectral broadening due to particle precipitation

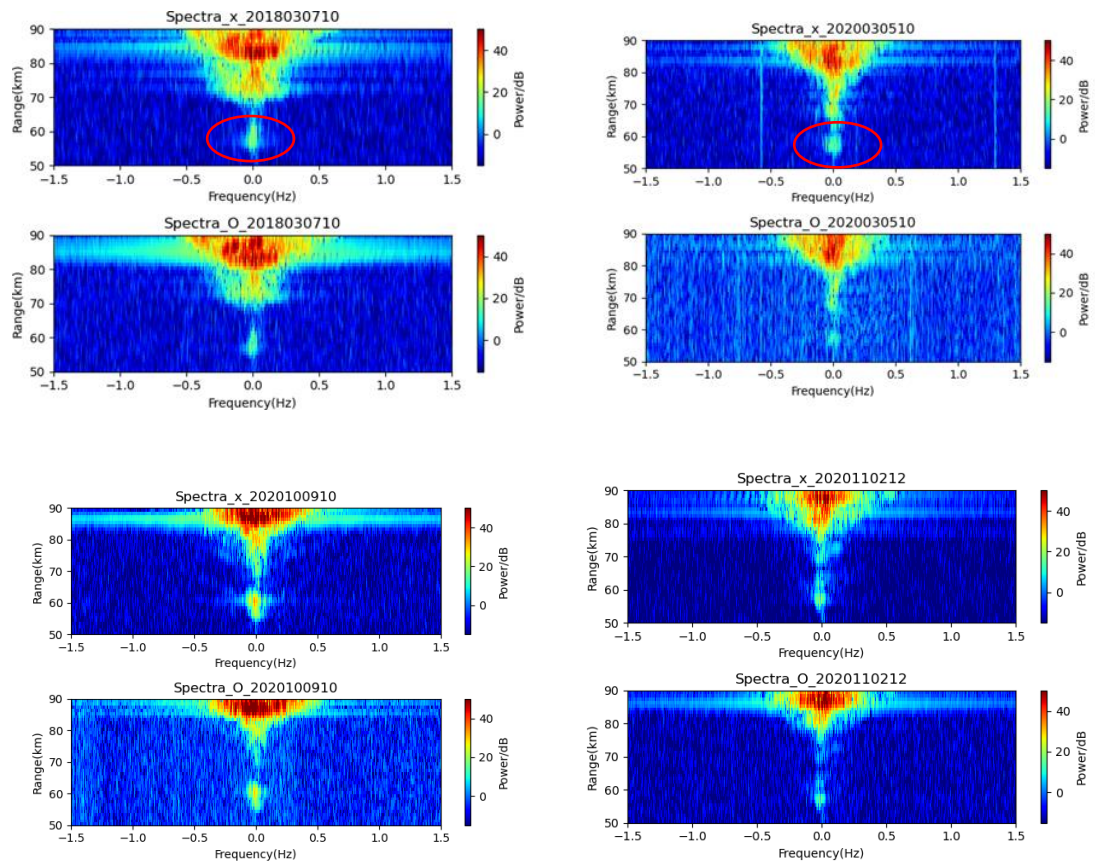
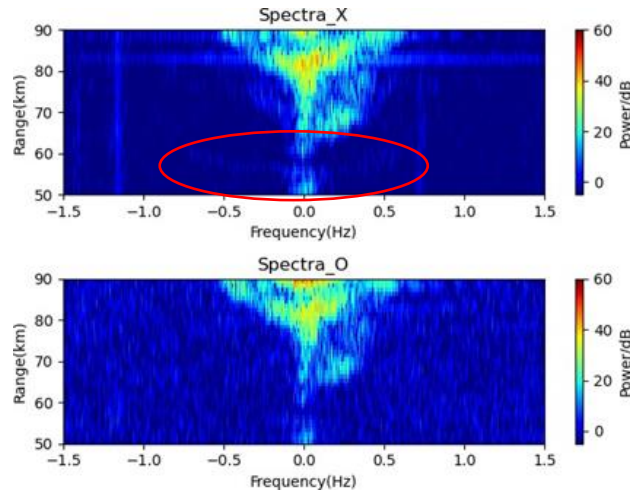


Figure 38: Isolated echoes at lower altitude without visible particle precipitation.

These spectra was generated for each hours in a day in which the layer was found and the observed details was entered in an excel sheet. A clear spectral arcs were visible on some days, which is an indication of particle precipitation (Figure 37). In some days multiple arc shaped components were seen because of different energies of the precipitating particles. As per the data set I have prepared, my findings are as follows:

The layers occurring can be classified into two

1. Layers seen with proper precipitation from the onset till the end.
2. Layers seen without precipitation from the onset till the end. In this case, no spectral arcs were seen, but only isolated echoes from the lower altitude.
3. Layers seen only at the middle of a period due to precipitation, where the onset and end of the period having no precipitation. In this case, the layer occurred has no relation with precipitation events, since the layer was present hours before visible precipitation. Hence, I categorized this under classification 2.



**Figure 39** : Multiple arcs in the spectra.

Sometimes multiple arcs were seen in the spectra. In Figure 39 one arc is visible at 66km altitude and a really isolated echo is seen around 52 km altitude. A mild indication of particle precipitation is seen here also, because a spectral arc is visible.

### 4.3.1 Unusual echoes seen in spectral analysis

During the analysis unusual spectral lines were visible in  $\pm 0.1$  Hz. This was similar to the echoes but not actually the original echo from the atmosphere. These were sea clutters and ground clutters, which is a common problem seen in the spectral analysis. The shift in frequency of the received echo signal due to the Doppler effect caused by a moving target allows a radar to separate desired moving targets (such as aircraft) from undesired stationary targets (such as land and sea clutter) even though the stationary echo signal may be many orders of magnitude greater than the moving target.

For an operational radar the back scattered transmitted signal may have interferences by the elements of the sea surface, these interfering signals are generally referred as sea clutter or sea echoes. Sea surface has a variety of features such as wedges, cusps, waves, foam, turbulence and spray as well as breaking events of all sizes and masses of falling water. These features contribute to the scattering of electromagnetic wave responsible for sea clutter. Mostly in this analysis these sea clutters were visible

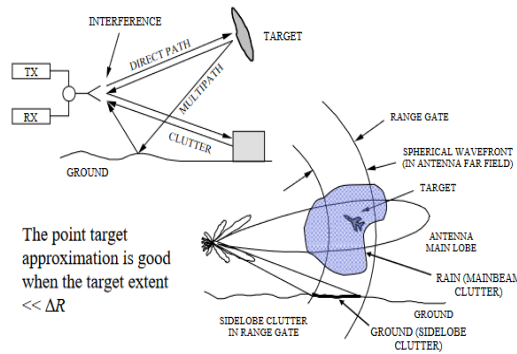


Figure 40: Clutter and Interferences. [12]

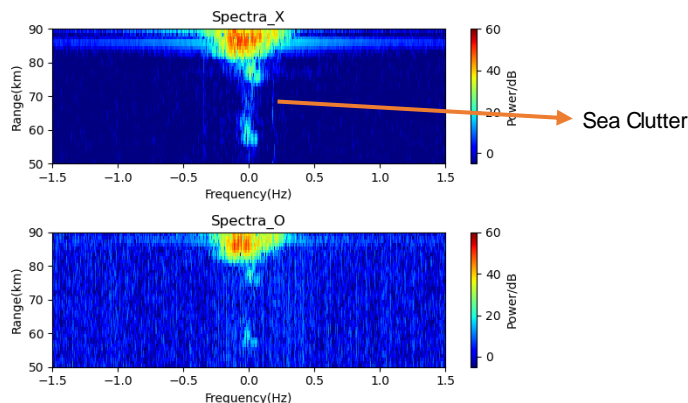


Figure 41: Sea clutter in spectra (2019/01/22 12:08UT)

4.4 Statistics

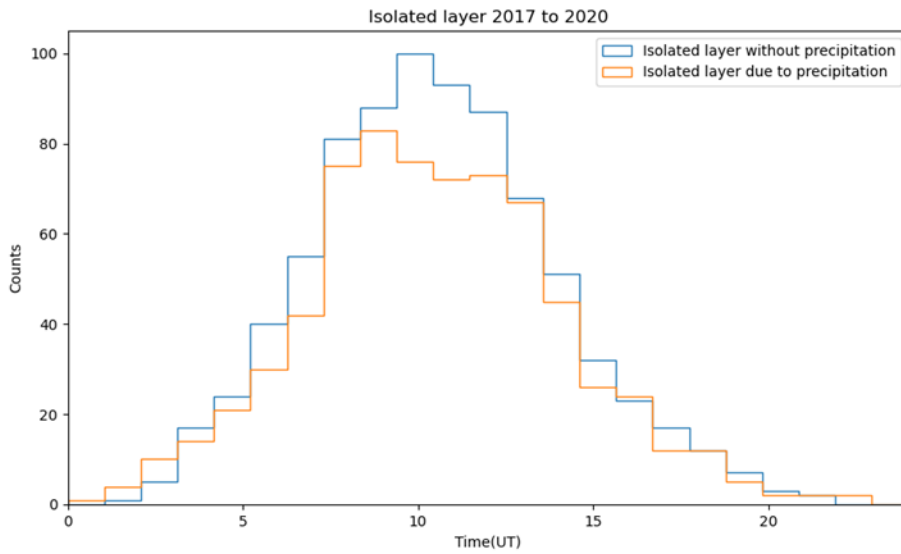


Figure 42: Isolated layer observed from 2017-2020

The results of the analysis by using raw data shows that the layers are seen mostly in the day time. The maximum number of layers were seen in between 9-13 UT. It is considered to be a day light phenomenon, since it maximizes around the noon. Hence, we can conclude that, the occurred isolated layers were modulated or controlled by the sun.

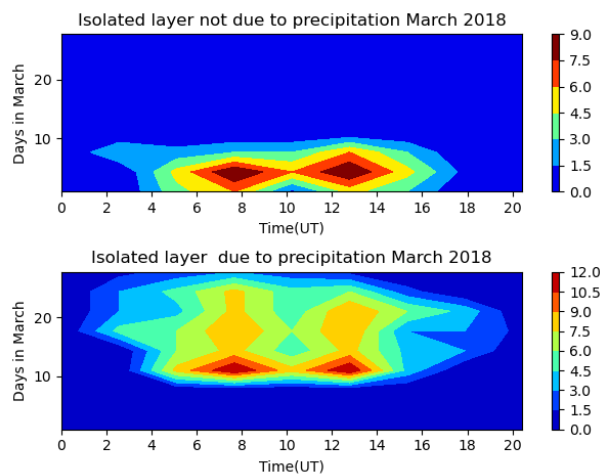
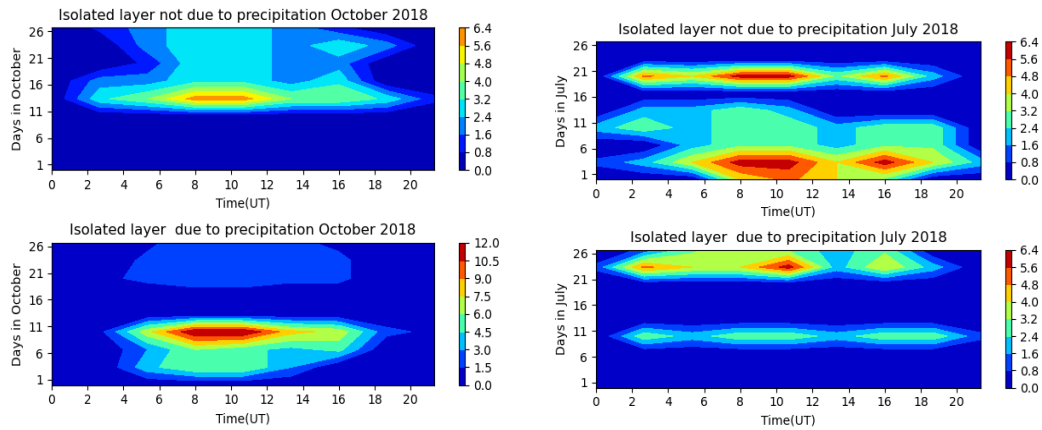


Figure 43: Isolated layers with and without precipitation seen on March 2018.

#### 4 Investigation of ionospheric layers by analyzing raw data



**Figure 44:** Isolated layer with and without particle precipitation observed on July and October 2018.

After checking the dataset of all the years, the layer occurred due to precipitation were mostly seen in spring and autumn. The layer occurred without precipitation was seen more in summer, may be because, during summer time the sun is above the horizon for a longer time. As a result of this, all the days in March, July and October for the year 2018 are statistically analyzed in detail. The statistics shows that during March and October the layer occurred due to precipitation was more and this contradicts the result obtained in July. The layer occurred without precipitation is more in summer time and it has no connection to precipitation events and it is mostly seen in sunlit periods.

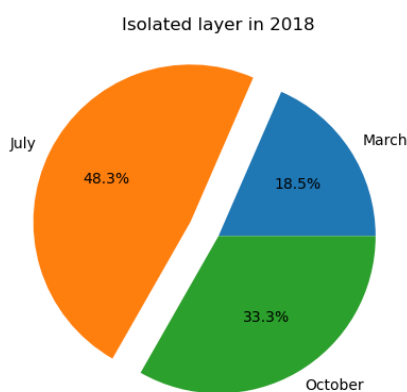


**Figure 45:** Isolated layer not related to precipitation for the three months in 2018 (March, July & October).

## 4.5 Cause of occurrence of isolated layers

### 4.5.1 Ground clutter

The Senja island which is located nearly 40-45 km away from the MF radar has a mountain of 500-600 m height. As explained in section 4.3.1 there is a chance of getting false echoes otherwise called ground clutters from these islands. The sun rises and heats up the lower ionosphere and sometimes the tropopause at 10-12 km altitude is occurred and scattering may occur at the tropopause. This is usually for very high frequency range. Even though we are using a medium frequency radar the possibility of tropopause scattering is checked. The scattered signal from the tropopause may hit this mountain and there might be a possibility of receiving these echoes by the radar. This echo fits nearly 60 km distance.

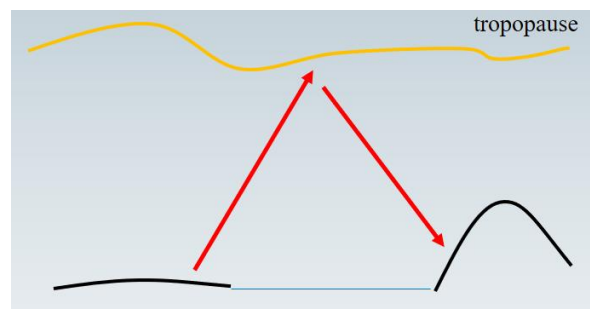


Figure 46: Tropopause scattering

According to the equation of refractive index in ionosphere [Balsely et.al.1980],

$$n - 1 = \underbrace{\frac{0.373 \cdot e}{T^2} + \frac{77.6 \cdot 10^{-6} Pa}{T}}_{\text{Neutral atmosphere}} - \underbrace{\frac{40.3 n_e}{f_0^2}}_{\text{Contribution of free electron in the ionosphere}}$$

Neutral atmosphere

Contribution of free electron in the ionosphere

$e(\text{mb})$  – partial pressure of water vapour

$P_a$ (mb) – Total atmospheric pressure

T (K) – absolute temperature

$f_0$ - Operating frequency

By calculating this, the electron density of D region, caused by ionization due to incident radiation of the sun, the backscatter is received at mesosphere height with a MF radar radar with 3MHz frequency is in the range of 1 for 50-60 km altitude [Balsley et.al.1980]. This means that there is no gradient of refractive index till 60 km altitude.(Figure 47 ). Therefore the electron density variation cannot be defined for 3 MHz frequency.

The changes in the altitude of tropopause is not equal to the change in the range of received echo. Therefore we can conclude that the echoes are receiving from the lower ionosphere and not due to scattering of tropopause. This can be further proved by checking the auto correlation of the radar echo.

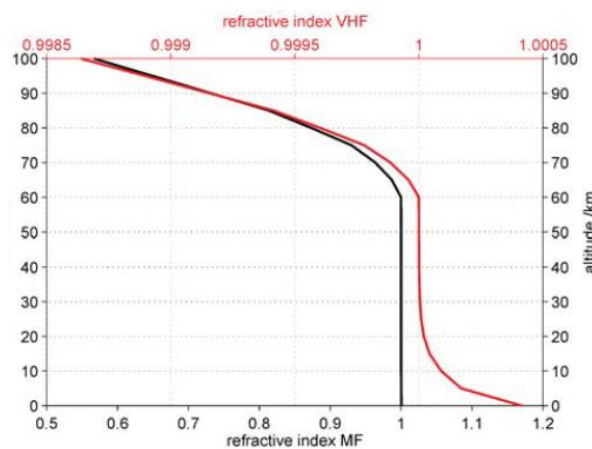


**Figure 47:** Refractive index of 3 MHz radar (Black). [25]

Auto correlation function is conducted by using the radar echoes. The time lag is analyzed by observing the phase and amplitude plot. If the auto correlation is narrow, then the correlation time is short and hence the target (layer) is short lived and vice versa. The flow chart (Figure 48) explains the algorithm used for the calculation and plotting of auto correlation.

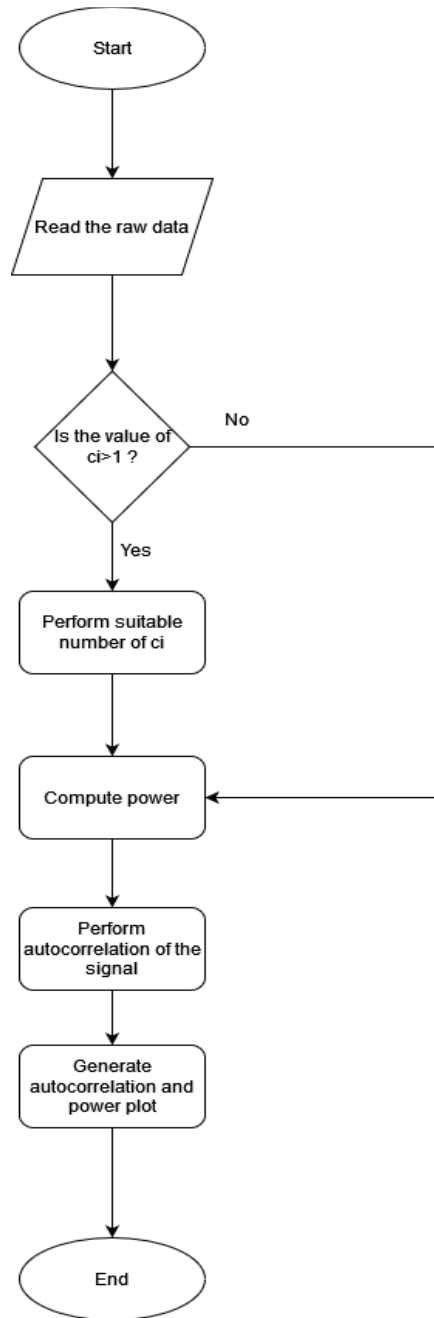


**Figure 48:** Flow chart for performing auto correlation.

As mentioned, the auto correlation and the power plots are generated. The complex radar raw data contains information about the power of O-mode and X-mode experimental values, times, the number of ranges, receivers, and samples used for the experiment. A suitable number of coherent integration is performed to improve the signal properties and the power is calculated. Auto correlation is performed for all the receivers and corresponding plots are observed.

#### 4 Investigation of ionospheric layers by analyzing raw data

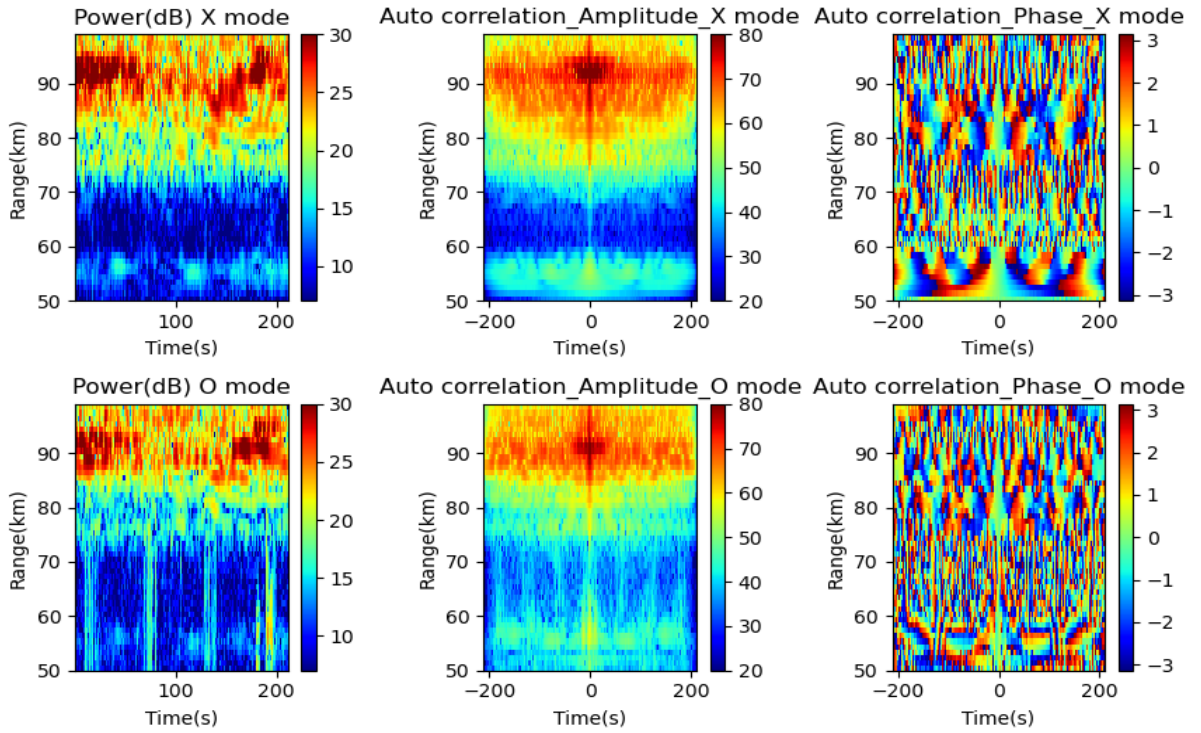


**Figure 49:** Auto correlation plots for the radar data taken on 09/10/2020 at 09:12 UT.

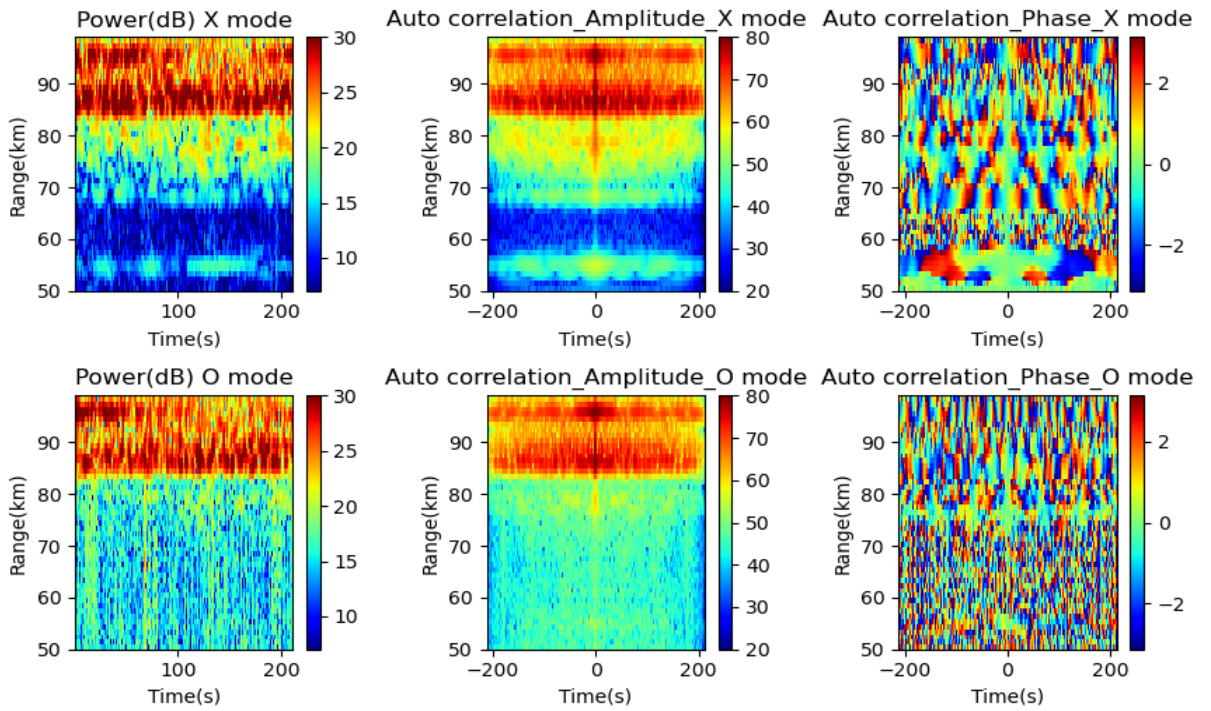


**Figure 50:** Auto correlation plots for the radar data taken on 18/10/2020 at 07:04 UT.

The power plots shows the presence of a layer in the range between 50-60 km altitudes. The auto correlation of radar echoes shows that the maximum power is seen at zero time lag. Since the correlation is done with same signal, it shows no time lag, but the width of the correlation gives information about the duration of the structure. The auto correlation observed in the plots is very broad showing a high electron density around these altitudes, which indicates longer correlation time and hence the structures seen around these altitudes are long lived. Hence, we can conclude that these strong echoes are receiving from the lower ionosphere.

#### 4.5.2 Radiation sources

Solar radiations penetrate below 85 km altitude and are Galactic and solar cosmic rays, Lyman  $\alpha$ , EUV, Solar X rays. They also contributes to ionization in the D region [Nath et.al. 1976]. The sunspot number index R gives the amount of solar activity. It measures the area of solar surface covered by spots. As the number of spot increases, magnetic complexity also increases and this results in large eruptive energy release known as solar flares.

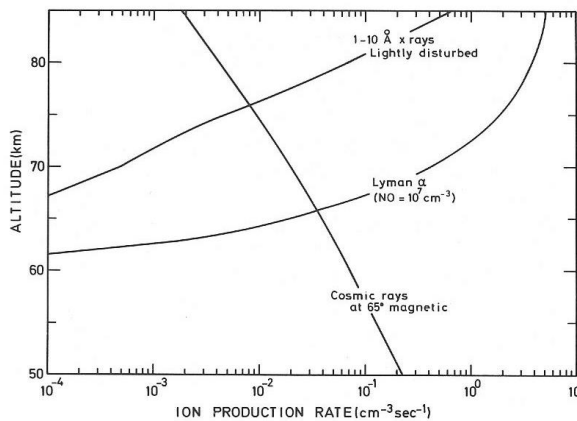


**Figure 51:** Penetration of cosmic rays to 50 km altitude.[27]

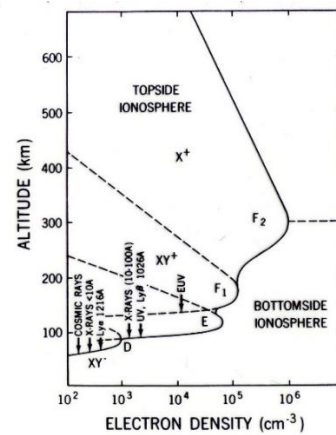


**Figure 52:** The principle sources of ionization at the lower part of ionosphere [28].

The cosmic rays down to lower D region are capable to ionize the molecular nitrogen and oxygen to form nitric oxides. The figure 51 and figure 52 shows that, the cosmic rays have a significant influence in the region of 50-60 km altitude. According to the

study of Thomas [1974]. The primary factor for ionization above 90km is due to solar UV radiations and X-ray. The ionization for a region range from 60-90 km is due to hard X-rays and Lyman  $\alpha$ . The region below 60km is ionized due to the effect of cosmic rays. From the auto correlation graphs, which is described in the previous section shows that the echo power coming from these altitudes are intense. Therefore, the cosmic ray radiation during the period of 2017-2020 was analyzed.

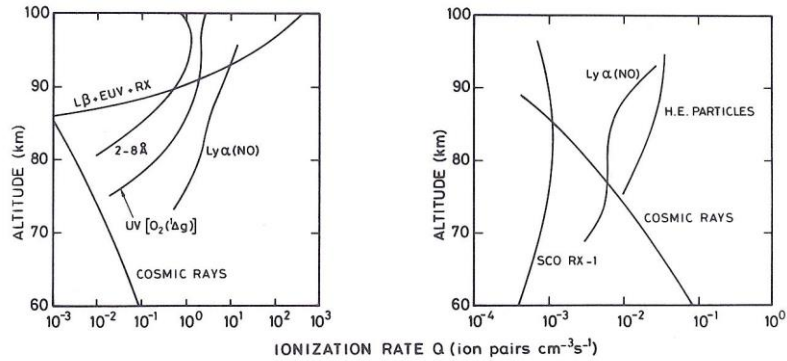


**Figure 53:** Ionization of various sources in the region from 60-100 km, during day and night [29]

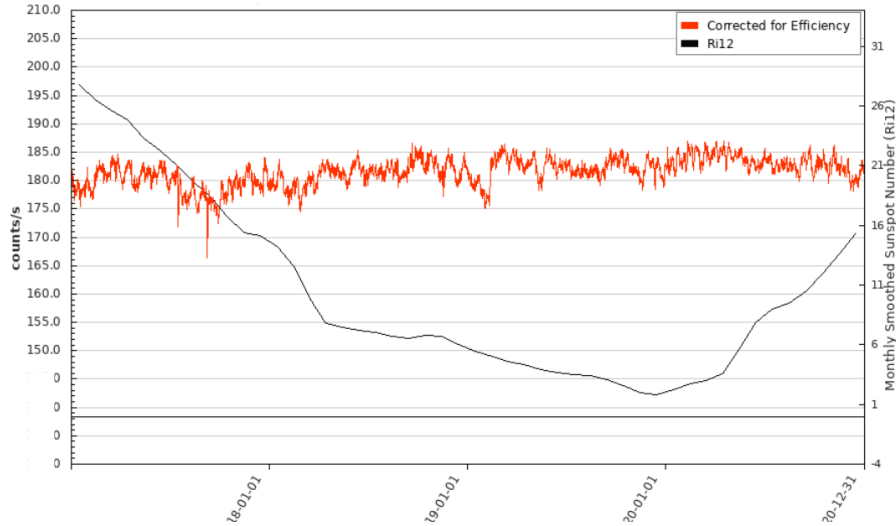


**Figure 54:** Galactic cosmic ray and sunspot number from 2017-2020. The sunspot number has an inverse relation to the detected cosmic rays. The plot was generated using NMDB online data access tool. [23]

The figure 54 gives information about the cosmic rays and the sunspot number (solar activity). Beginning from 2017 to the mid of 2020, there is a drop in the solar activities and the Galactic cosmic rays at these times were checked and the result shows that, when there is an increase in cosmic radiations, the sunspot number decreases and vice versa. During these times, the presence of isolated layers at lower altitude that is, 50-60 km altitude was found more (Figure 42). Hence, it can be concluded that the occurrence of these layers has an influence of cosmic rays. The Figures 55 shows that, the cosmic radiation in July was very high. At the same time the layer not connected to precipitation that is observed from the original radar raw data also have a very high count rate.

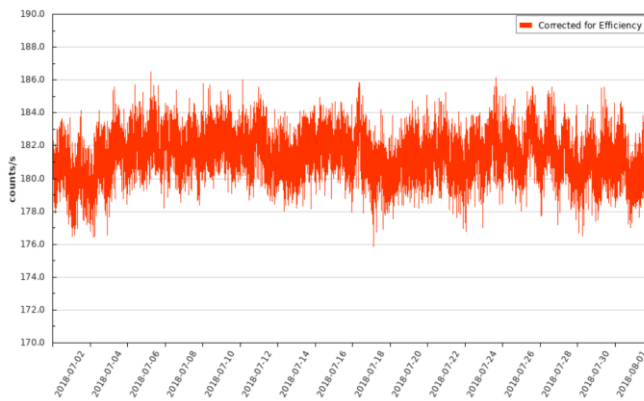


Figure 55: Cosmic rays observed in July 2018. [23]

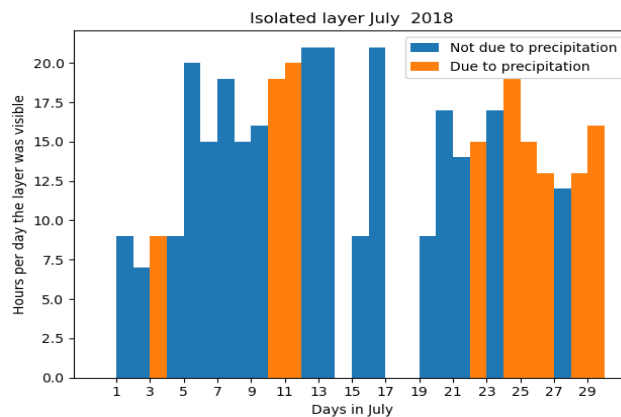
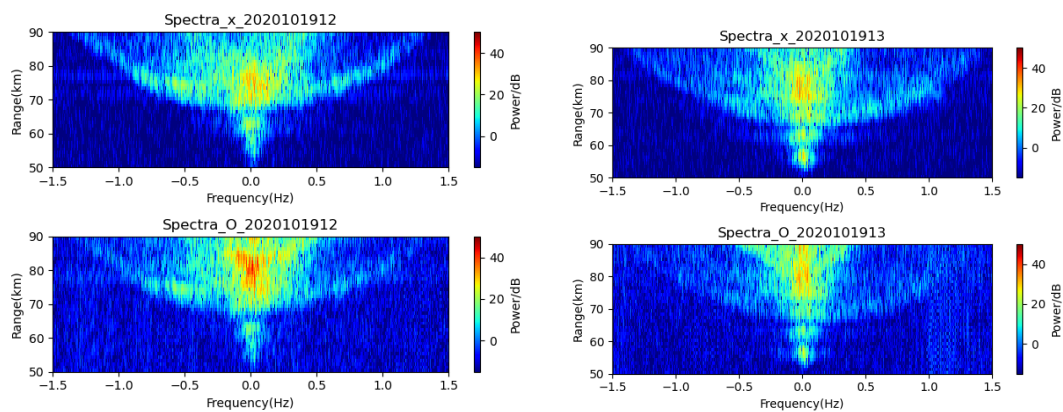


Figure 56: Counts of isolated layer present in July 2018.

## 5 Broadening of spectral arc

The radar target in the middle atmosphere is drifted due to background wind. Due to horizontal wind, a few portion of the precipitated particles may move towards or away from the radar which will give a positively or negatively Doppler shifted spectral component. The relative motion of the target is obtained by the detected Doppler shift within the frequency domain. Beam broadening effect has a profound influence on the measured Doppler spectrum, mainly governed by mean background wind [Chue ,2002].



**Figure 57:** Broadened spectral arc.

For the atmospheric measurements, the wind field is assumed to be homogeneous and the precipitated particles, which are the targets with respect to the radar are moving in this homogeneous medium. The radial velocity is measured for each beam pointing direction towards the target. Because of the movement of the target, the range from the radar will increase resulting in the increase of radial velocity component of the horizontal wind. This makes an arc like shape to the spectra.

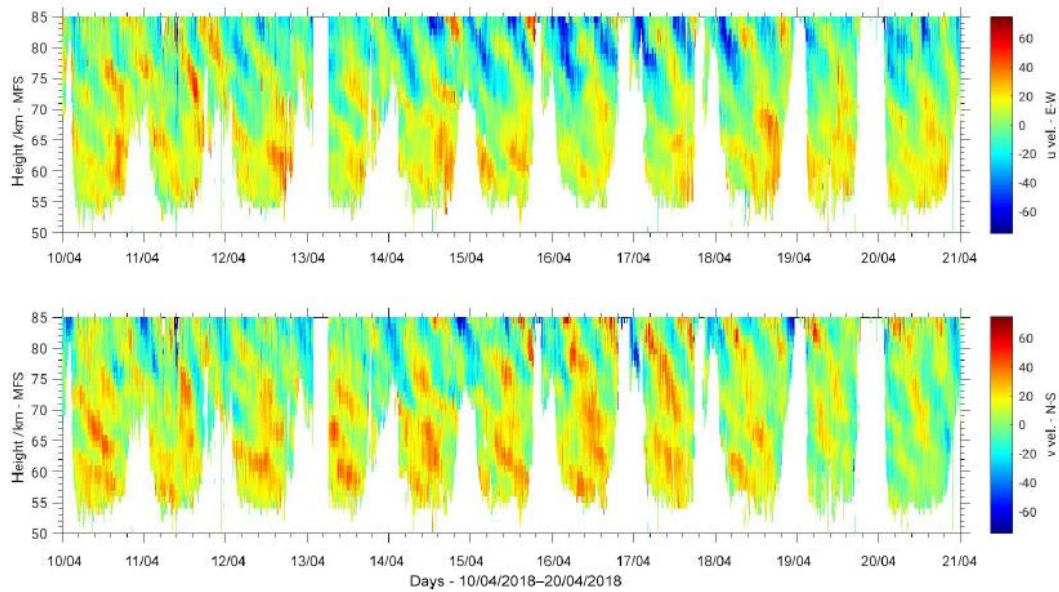


**Figure 58:** Horizontal wind measured by the Saura Mf radar in April 2018 [31].

As mentioned earlier, Saura MF can be used to measure electron density and wind in middle atmosphere (50- 90 km altitude). It is operated with five beam scanning experiment, a vertical and four oblique beam directions. Both extra ordinary and ordinary modes were probed during these times. The run time of the experiment was 220s, with 100Hz pulse repetition frequency and to increase the average output power and to neglect the interferences, a four bit complementary code was used which requires two coherent integrations. After that, Doppler beam swinging method (DBS) was applied to derive the horizontal and vertical wind fields. The experimental length is typically 12 minutes, which is the minimum temporal wind resolution corresponding to the experimental length.

The wind estimation from the Saura MF shows (Figure 58) the presence of wind in between 50 to 85 km altitude. The observation of wind was partially around 50 km altitude and very high in 60-80 km altitude. [Ralph et.al.,2019]

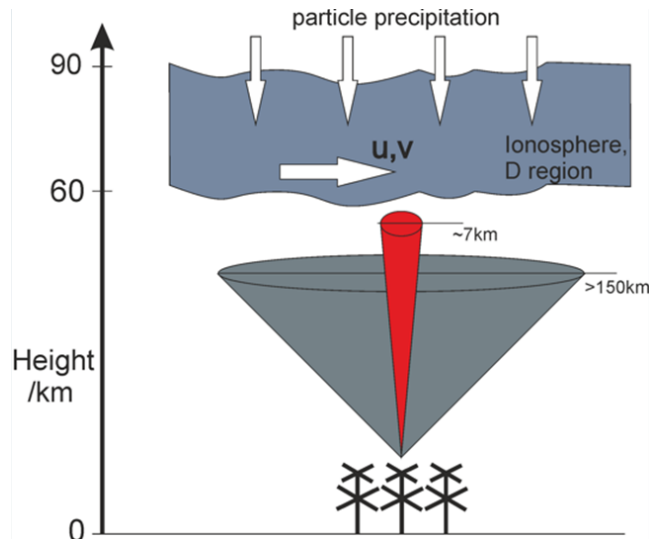


**Figure 59:** Schematic of particle precipitation events as seen by the Saura radar. [31]

The narrow red conical shape indicates the radar beam volume during quiet geomagnetic condition and the enlarged grey portion indicates the increasing volume of the scattered radar beam during the particle precipitation events. [Ralph et.al.,2019]

### 5.1 Wind measurement technique

The Doppler beam swinging method (DBS) is a technique commonly used for wind measurement in the atmosphere. This method assumes that multiple and well distributed target exists and are drifting within a homogeneous medium. DBS method uses different oblique beams into individual pointing direction of the radars and from this the radial velocity of the target is measured, and these beam are combined with the direction of measurement to derive horizontal and vertical winds. The vertical velocity can be obtained directly from the vertical beam. Horizontal wind velocity can be derived using different beam configuration. This technique helps to find east west and vertical component of wind from the radial wind velocities along at least three non collinear narrow beams. Accuracy of the wind estimation depends on the system of observation and atmospheric conditions. The wind estimate from four beam configuration has better results than the two and three beam configuration [Rao et.al.2008].

According to Woodman and Guillen [1974], the five beam configuration gives accurate results when compared to the three beam configuration.

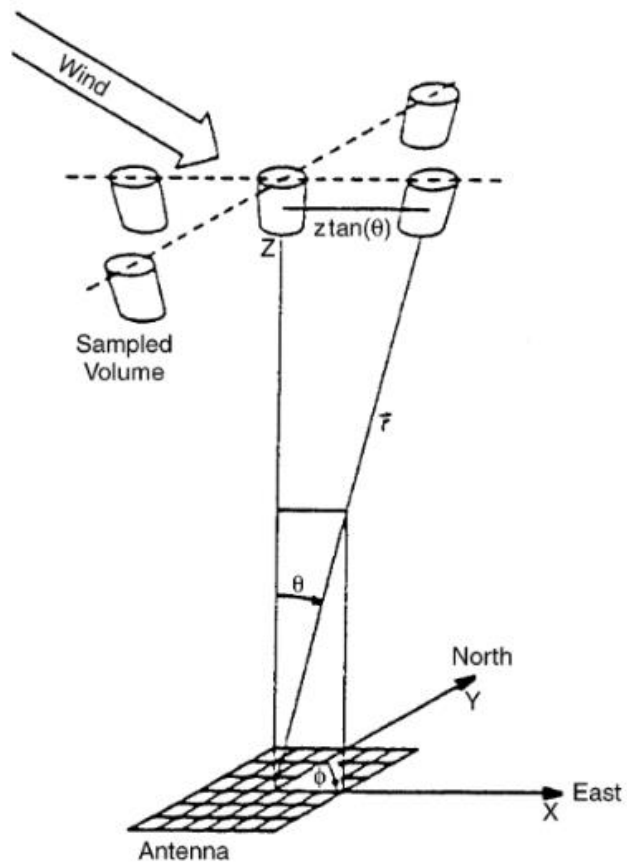


**Figure 60:** Doppler beam swinging (DBS) technique for wind measurement with a five beam configuration. The altitude, range and zenith angle are denoted by  $z$ ,  $r$  and  $\theta$  respectively. [32]

## 5.2 Calculation and Comparison of horizontal wind on spectra

In this section the relation of magnitude of the horizontal wind to the spectral arc is described. The horizontal wind has two components  $u$  and  $v$ . The magnitude of the horizontal wind is calculated by using Pythagorean Theorem,  $\sqrt{u^2+v^2}$ . Then the relative Doppler frequency of the horizontal wind velocity is calculated (by subtracting the radar frequency to the calculated Doppler frequency). This velocity of horizontal wind is cross checked with the observed spectra.

### Case 1

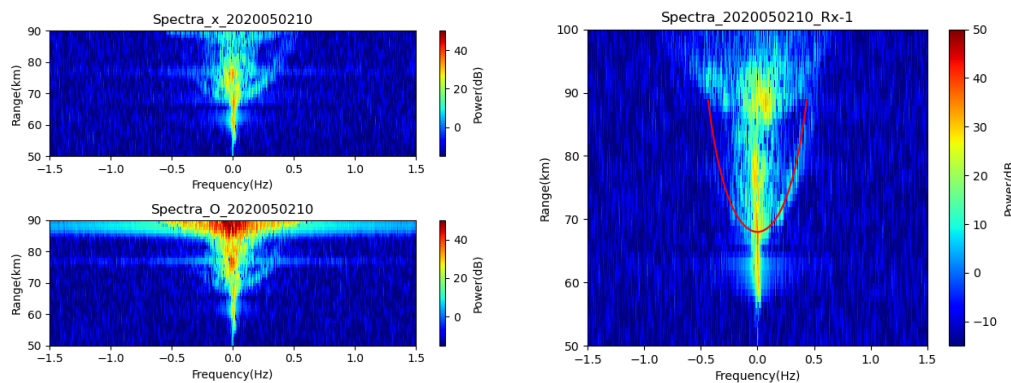


**Figure 61:** Spectra obtained on 2<sup>nd</sup> May 2020(left) and the matching of estimated wind (red arc) with the spectral arc for X-mode (right).

The spectra for 02 May 2020 at 10:00 UT are shown in figure 61. In this, an arc shape is seen with a bottom height of 69 km altitude at 0 Hz Doppler frequency extending to higher altitude range of around 90km with a Doppler frequency of +0.4Hz. This arc is believed to be occurred because of particle precipitation event. The radar volume increases at very high altitude so the measurement above 85 km is not considered. Saura DBS hourly data has a reasonably good result below 85 km altitude [Wilhelm et al.2017] The magnitude of the horizontal wind velocity and the relative Doppler frequency are calculated and checked whether it fits at 69 km altitude or not. The result is shown in the right panel of figure 61 and it shows that the echo power perfectly fits the magnitude of horizontal wind velocity. Many similar situations were tested and the estimated wind perfectly matched with the spectral arc. Hence, I can conclude that this horizontal wind velocity have an influence in the spectral arc.

Case 2

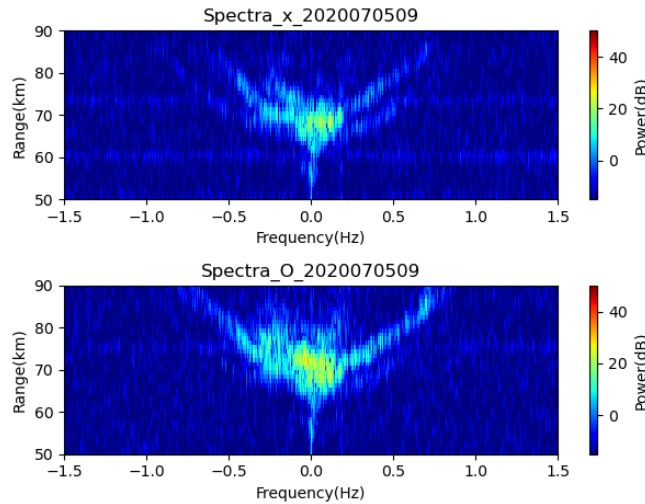


Figure 62: Spectra obtained for 5<sup>th</sup> May 2020 at 9:04 UT.

When there is only single spectral arc, the estimated wind velocity perfectly fits the arc. There are conditions where multiple arcs were seen in the spectra. For instance, the spectra obtained for 5<sup>th</sup> May 2020 at 09:48 UT shows that two precipitation events with different energies are formed one at 66km altitude and the other at 70 km altitude. Similar to the previous case, checked whether the simulated Doppler shift for the estimated wind velocity matches the spectral arcs. The spectral arc at 66km altitude is represented by red colored arc and the other with black and it matched with the spectral arc.

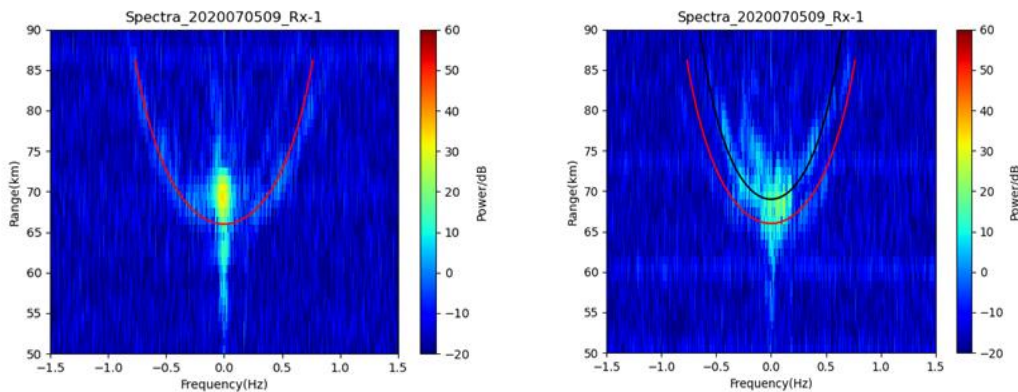
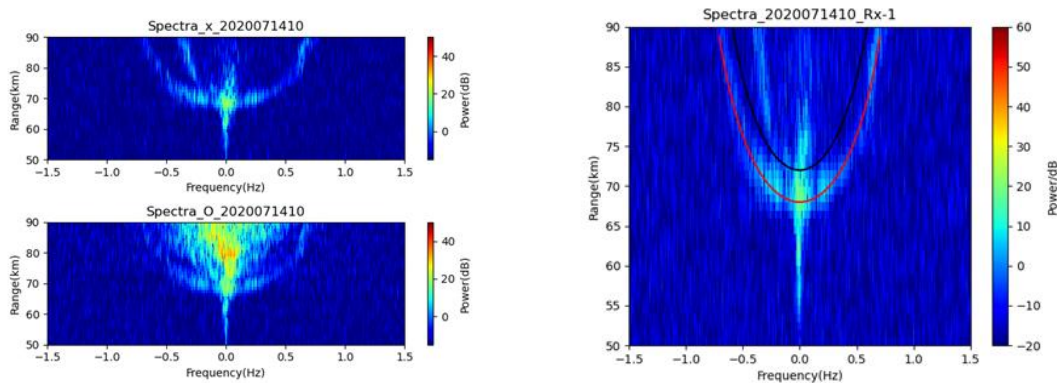


Figure 63: Estimated wind calculations (red) for the observed multiple arcs (Precipitation with different energies).

### 5.3 Potential errors in wind measurement

Estimated winds sometimes tends to show incorrect values and these erroneous wind measurements are described with example in this section. As we know that the radiation pattern get wide due to particle precipitation and this increase in spectral width is in relation to magnitude of horizontal wind velocity. If the wind estimation does not work properly then the winds data contains errors, as we couldn't assume the spectrum is false since it is taken from the original radar raw data. The particle precipitation may affect and impair wind estimation. So, if the estimated winds tend to show incorrect values during particle precipitation events and if this estimate is not consistent to the DBS wind value, the DBS should be flagged as not reliable.



**Figure 64:** Mismatch of estimated wind with the spectral arcs.

In this example (Figure 64), two spectral arcs are seen in different altitudes at 69 and 73km with two different wind velocities. The estimated wind fits the lower altitude (69 km) closely, but in upper altitude it doesn't fit, as the Doppler estimation at upper altitude are contaminated by particle precipitation events at the lower altitude.

Wind is calculated from DBS and spectra was generated for every beam pointing and then the Doppler shift is estimated. In this case, there is two maximum and so the Doppler shift can be very symmetric. In DBS experiment, the radial velocity of the wind from these altitude is calculated for the wind inversion at the end (5 beam direction). These five beam directions are inverted to horizontal and vertical wind. If these radial velocity are wrong then the wind datas are wrong as well.

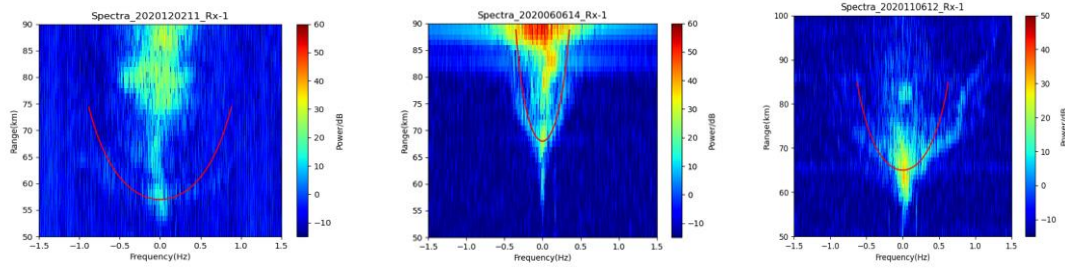


Figure 65: Wrong wind measurements.

Also, there may be situations in which no detected echo power at the center of the spectrum. This may happen, when the vertically emitted and potentially reflected wave is highly attenuated. This may also spoil the Doppler shift estimation.

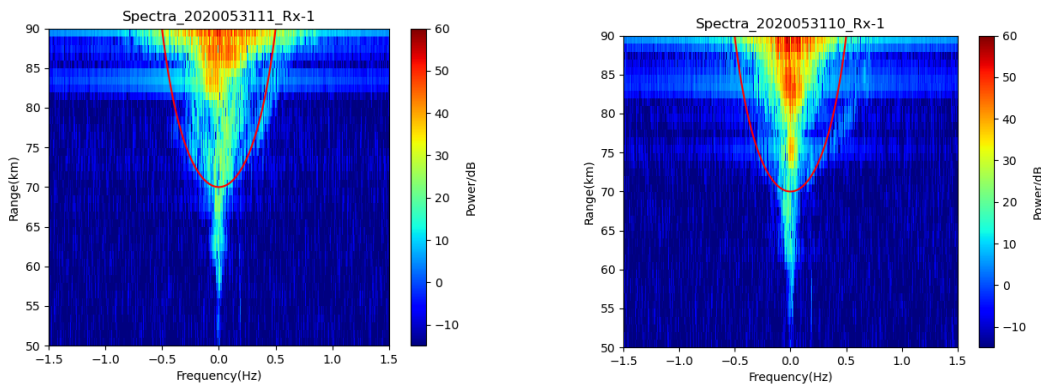
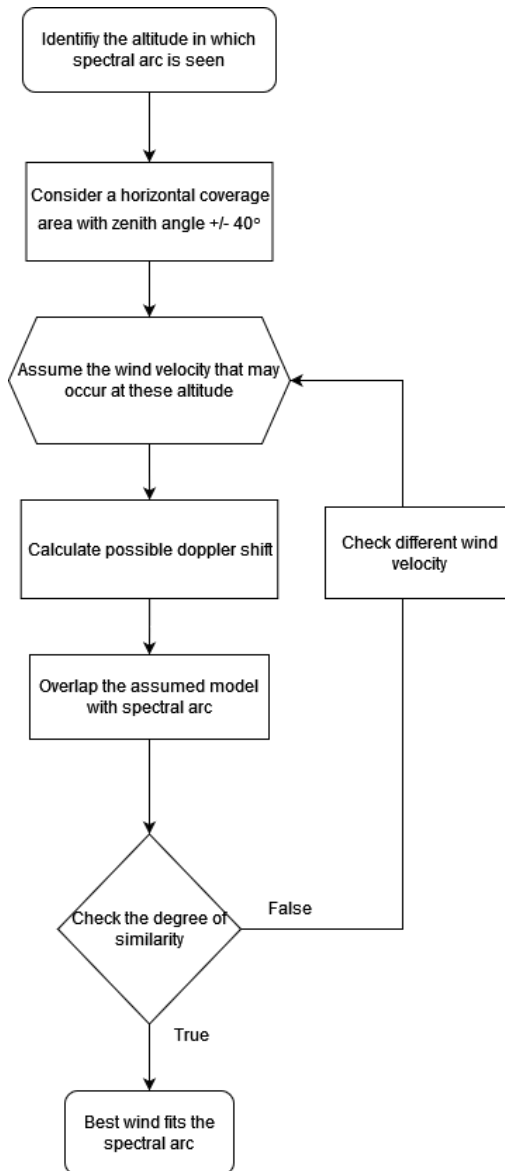


Figure 66: Mismatch observed in estimated winds at 10:00 and 11:00 UT

In this example on 31<sup>st</sup> May 2020 (Figure 66), the precipitation event was persistent, and so the spectral arcs were present at 10:00UT and 11:00 UT at same altitude but the wind estimation at 10:00 UT shows erroneous result whereas in 11:00UT shows more accurate result. From these examples, I conclude that there are probability in getting errors in the DBS wind data.

### 5.3.1 Solution to wind correction

As I have stated in the above section, there are possibilities for errors in the wind data. In order to avoid these errors, we can use the below mentioned solutions.



**Figure 67:** Wind correction technique.

This detection process can be done earlier, when and at which base altitude these spectral arc would occur. During that time the altitude can also be iterated for checking the best fit of estimated wind to spectra.

---

## 6 Conclusions and summary

The relation of energetic particle precipitation with the layer formation in lower ionosphere is investigated in this work. During high solar activities, the highly energetic protons causes precipitation and layers from very low altitude are visible. In this study, these high energetic solar proton events are purposefully eliminated and low energetic particle like auroral and radiation belt electrons are considered. The solar proton events are very rare and the latter is more frequently observed. Medium frequency Saura MF radar is used for this study, because of its high sensitivity to solar and geomagnetic activities.

During the geo-magnetically disturbed days, because of high ionization most of the echoes at higher altitude vanishes and a thin layer can be seen around 60-65 km altitude, which is termed as Isolated Lower Mesospheric Echoes. For some days, significant ionization was observed below normal D region altitude due to particle precipitation and these ILME events can be seen as low as 50km altitude, which can be considered as C layer. In 2017, very high series of geomagnetic storm was observed and the ILME occurrence seems to be very high during this year. In all the other years, the occurrence is found to be around 40%. The events are seen more around the equinoxes (spring and autumn) and daylight hours.

A study with raw data come to an end that there are echoes seen at lower altitude (50-60km) without obvious precipitation events in higher altitude. For many days, these echoes at lower altitude was present all day long. These phenomenon was mostly observed in summer season, may be due to the relentless behavior of sun during this season. Thus we can conclude that this C layer is persistent even without much particle precipitation, but the cosmic radiations plays a significant role in the formation of C layer. These cosmic ray penetrate to lower ionosphere and performs ionization. Thereby increasing the electron density.

In a nutshell, when comparing the wind estimation to the generated spectra from raw data, it is obvious that the background wind has a relation with particle precipitation. The background wind broadens the spectral arc as the magnitude of the calculated wind velocity matches the spectral arc occurred due to particle precipitation

---

The wind data taken from DBS experiments are not fully reliable as it shows errors. The reason for this may be the failure in Doppler shift estimation. This errors in the wind measurement can be eliminated by assuming a horizontal coverage ( $\pm 40^\circ$  zenith angle) around the precipitation area. Thereafter applying a trial and error method by varying the possible wind velocity and altitude.

---

## List of figures

<b>Figure 1</b> : Temperature and electron density.....	6
<b>Figure 2</b> : Division of ionosphere regions by electron density .....	7
<b>Figure 3</b> : Regions of the ionosphere showing the D, E and F layer .....	8
<b>Figure 4</b> : Charged electrons in Earth's magneto tail .....	9
<b>Figure 5</b> : Northern light seen in western Canada .....	9
<b>Figure 6</b> : Pulse reflected and 6km thick layer of ionization .....	10
<b>Figure 7</b> : weak reflections from altitude below the normal D-Region .....	10
<b>Figure 8</b> : Data obtained from Saura MF radar showing the D, E, F regions .....	11
<b>Figure 9</b> : Simple block diagram of a radar .....	12
<b>Figure 10</b> : The Electromagnetic spectrum .....	13
<b>Figure 11</b> : The Saura MF radar.....	13
<b>Figure 12</b> : Schematic structure of the Saura MF radar.....	14
<b>Figure 13</b> : Energetic particle precipitation .....	16
<b>Figure 14</b> : EPP impact on the atmosphere .....	17
<b>Figure 15</b> : Ionization rate of EPP .....	18
<b>Figure 16</b> : Flow chart for generating daily power plots. ....	19
<b>Figure 17</b> : Block diagram of the analysis procedure. ....	20
<b>Figure 18</b> : Power plot of a quiet day.....	20
<b>Figure 19</b> : Power plot of a disturbed day. ....	21
<b>Figure 20</b> : Flow charts for calculating the ILME events. ....	23
<b>Figure 21</b> : Monthly power profile for quiet days.....	24
<b>Figure 22</b> : Annual occurrence of ILME events (2017 to 2020) .....	25
<b>Figure 23</b> : Particle precipitation events obtained for 2018. ....	26
<b>Figure 24</b> : ILME events in 2017. ....	27
<b>Figure 25</b> : Annual particle precipitation events (2003 to 2016) .....	28
<b>Figure 26</b> : Observed ILME events in the current study. ....	28
<b>Figure 27</b> : Relation between the Kp index and ionospheric conditions .....	29

---

<b>Figure 28</b> : The Kp index from the year 2017 to 2020 .....	30
<b>Figure 29</b> : Layer present at lower altitude seen in the power plots.....	31
<b>Figure 30</b> : Simulated radiation pattern of the Saura MF radar .....	32
<b>Figure 31</b> : Flow chart for the analysis of isolated layers by raw data. ....	33
<b>Figure 32</b> : DMF migration cycle .....	34
<b>Figure 33</b> : DMF before migrating data .....	36
<b>Figure 34</b> : DMF after data migration and freeing space .....	36
<b>Figure 35</b> : Spyder window .....	37
<b>Figure 36</b> : Raw data block of x-mode power .....	38
<b>Figure 37</b> : Spectral broadening due to particle precipitation .....	39
<b>Figure 38</b> : Isolated echoes at lower altitude without visible PP.....	39
<b>Figure 39</b> : Multiple arcs in the spectra. ....	40
<b>Figure 40</b> : Clutter and Interferences .....	41
<b>Figure 41</b> : Sea clutter in spectra .....	41
<b>Figure 42</b> : Isolated layer observed from 2017-2020.....	42
<b>Figure 43</b> : Isolated layers with and without precipitation on March(2018).....	42
<b>Figure 44</b> : Isolated layer observed on July and October 2018. ....	43
<b>Figure 45</b> : Isolated layer not related to precipitation in 2018(3 months).....	43
<b>Figure 46</b> : Tropopause scattering.....	44
<b>Figure 47</b> : Refractive index of 3 MHz radar (Black) .....	45
<b>Figure 48</b> : Flow chart for performing auto correlation. ....	46
<b>Figure 49</b> : Auto correlation plots for the radar data.....	47
<b>Figure 50</b> : Auto correlation plots for the radar data.....	47
<b>Figure 51</b> : Penetration of cosmic rays to 50 km altitude.....	48
<b>Figure 52</b> : The principle sources of ionization at the lower ionosphere.....	48
<b>Figure 53</b> : Ionization of various sources in the region from 60-100 km.....	49
<b>Figure 54</b> : Galactic cosmic ray and sunspot number from 2017-2020 .....	49
<b>Figure 55</b> : Cosmic rays observed in July 2018. ....	50
<b>Figure 56</b> : Counts of isolated layer present in July 2018. ....	50
<b>Figure 57</b> : Broadened spectral arc .....	51

---

<b>Figure 58:</b> Horizontal wind measured by the Saura Mf radar .....	52
<b>Figure 59:</b> Schematic of particle precipitation events as seen by the Saura .....	53
<b>Figure 60:</b> Doppler beam swinging (DBS) technique .....	54
<b>Figure 61:</b> Spectral arc and the matching of estimated wind .....	55
<b>Figure 62:</b> Spectra obtained for 9 <sup>th</sup> May 2020 at 9:04 UT. ....	56
<b>Figure 63:</b> Estimated wind calculations for the observed multiple arcs.....	56
<b>Figure 64:</b> Mismatch of estimated wind with the spectral arcs. ....	57
<b>Figure 65:</b> Wrong wind measurements. ....	58
<b>Figure 66:</b> Mismatch observed in estimated winds at consecutive times .....	58
<b>Figure 67:</b> Wind correction technique. ....	59

---

## List of Tables

<b>Table 1:</b> Technical parameters of Saura MF.....	15
<b>Table 2:</b> Commands used for operating DMF system. ....	35

---

## List of Abbreviations

AOA	Angle of Arrival
CME	Coronal Mass Ejection
DBS	Doppler Beam Swinging
DPE	Differential Phase Experiment
DAE	Differential Amplitude Experiment
DMF	Data Migration Facility
DMAPI	Data Management Application Programming Interface
EPP	Energetic Particle Precipitation
EM wave	Electro Magnetic waves
FFT	Fast Fourier Transform
GCRs	Galactic Cosmic Rays
HO <sub>x</sub>	Hydrogen Oxides
HDF5	Hierarchical Data Format version 5
IF	Intermediate Frequency
IMF	Interplanetary Magnetic Field
ILME	Isolated Lower Mesospheric Echoes
IAP	Leibniz-Institut für Atmosphärenphysik
KE	Kinetic Energy
MF	Medium Frequency
MST	Mesosphere-Stratosphere-Troposphere
NO <sub>x</sub>	Nitrogen Oxides
O-Mode	Ordinary Mode

---

O <sub>3</sub>	Ozone
PP	Particle Precipitation
PPE	Particle Precipitation Events
PRF	Pulse Repetition Frequency
RADAR	Radio Detection And Ranging
SPE	Solar Proton Event
Sqrt	Square root
UV ray	Ultra Violet ray
UHF	Ultra High Frequency
UT	Universal Time
VLF	Very Low Frequency
VHF	Very High Frequency
X-Mode	Extra Ordinary Mode

---

## List of references

- [1] Wikipedia: Electron density at Ionosphere. <https://en.wikipedia.org/wiki/Ionosphere>.
- [2] Randy Russell : UCAR, Center for science education : The ionosphere URL: <https://scied.ucar.edu/learning-zone/atmosphere/ionosphere> , Accessed on September, 2021
- [3] NASA. The moon and the magneto tail. URL: [https://www.nasa.gov/topics/moonmars/features/magnetotail\\_080416.html](https://www.nasa.gov/topics/moonmars/features/magnetotail_080416.html) , Accessed on September, 2021
- [4] Elvis Mason: URL: <https://www.cbc.ca/news/canada/manitoba/northern-lights-manitoba-1.6208770>. Accessed on October,2021
- [5] J.E. Rasmussen, P.A. Kossey, E.A. Lewis. [1980]: Evidence of an ionospheric reflecting layer below the classical D region. URL: <https://agupubs.onlinelibrary.wiley.com/doi/abs/10.1029/JA085iA06p03037>
- [6] W.C.Bain and B.R. May [1967]: D region electron density distribution from propagation data. <https://doi.org/10.1049/piee.1967.0306>.
- [7] M. Nicolet, A.C. Aikin [1960]: The formation of the D region of the ionosphere. <https://doi.org/10.1029/JZ065i005p01469>.
- [8] Krasnushkin, P.E [1962]: On the propagation of long and very long radio waves around the Earth. *Supplemento Nuovo Cimento*, 26(1), 50-112. <https://doi.org/10.1007/BF02782993>.
- [9] Renkwitz, Latteck.R [2017]: Variability of virtual layered phenomena in the mesosphere observed with medium frequency radars at 69°N. *Journal of Atmospheric and Solar Terrestrial Physics*. Vol.163, Pages 38-45. [10.1016/j.jastp.2017.05.009](https://doi.org/10.1016/j.jastp.2017.05.009).
- [10] Merrill I. Skolnik [1990]: Radar handbook.
- [11] Balsley, B.B., Gage, K.S. The MST radar technique: Potential for middle atmospheric studies. *PAGEOPH* 118, 452–493 (1980). <https://doi.org/10.1007/BF01586464>.
- [12] Prof. David Jenn: Radar Fundamentals URL <https://faculty.nps.edu/jenn/Seminars/RadarFundamentals.pdf>.
- [13] IAP, Homepage. The Saura MF Radar: URL <https://www.iap-kborn.de/forschung/abteilung-radarsondierungen/instrumente/mf-radare/saura-mf-radar/>. Accessed on May, 2021.
- [14] Sinnhuber, M., Nieder, H. & Wieters, N [2012]. Energetic Particle Precipitation and the Chemistry of the Mesosphere/Lower Thermosphere. *Surv Geophys* 33, 1281–1334. <https://doi.org/10.1007/s10712-012-9201-3>.
- [15] Seppälä, A., Matthes, K., Randall, C.E. et al [2014]. What is the solar influence on climate? Overview of activities during CAWSES-II. *Prog. in Earth and Planet. Sci.* 1, 24. <https://doi.org/10.1186/s40645-014-0024-3>.
- [16] A. Seppälä, M.A. Clilverd, M. J. Beharrell, C. J. Rodger, P.T. Verronen, M.E. Andersson, D.A. Newnham [2015]: Substorm induced energetic electron precipitation: impact on atmospheric chemistry, *Geophys. Res. Lett.*, 42, 8172–8176 <https://doi.org/10.1002/2015GL065523>.
- [17] Cora Randall: CEDAR Meeting [2010]. Atmospheric coupling via energetic particle precipitation  
URL: [https://cedarweb.vsp.ucar.edu/wiki/images/d/d2/Randall\\_ppt\\_turbopause.pdf](https://cedarweb.vsp.ucar.edu/wiki/images/d/d2/Randall_ppt_turbopause.pdf)., Accessed on July, 2021.

- 
- [18] Lina Tran: NASA homepage. September 2017's Intense solar activity viewed from space  
URL <https://www.nasa.gov/feature/goddard/2017/september-2017s-intense-solar-activity-viewed-from-space>, Accessed on October 2021.
- [19] AGU Advancing earth and space science: Space weather events of 4- 10 September 2017: [https://agupubs.onlinelibrary.wiley.com/doi/toc/10.1002/\(ISSN\)1542-7390.SW-SEPT2017](https://agupubs.onlinelibrary.wiley.com/doi/toc/10.1002/(ISSN)1542-7390.SW-SEPT2017) .Accessed on October, 2021
- [20] C.M. Hall, A.H. Manson, C.E. Meek, S. Nozawa [2006] : Isolated lower mesospheric echoes seen by medium frequency radar at 70°N, 19°E Atmos. Chem. Phys., 6, 5307–5314,  
<https://doi.org/10.5194/acp-6-5307-2006>
- [21] Menvielle M., Iyemori T., Marchaudon A., Nosé M. [2011]: Geomagnetic Indices. In: Mandaia M., Korte M. (eds) Geomagnetic Observations and Models. IAGA Special Sopron Book Series, vol 5. Springer, Dordrecht.  
[https://doi.org/10.1007/978-90-481-9858-0\\_8](https://doi.org/10.1007/978-90-481-9858-0_8).
- [22] VK3FS. Home pages: 3 band condition indicators URL <https://3fs.net.au/making-sense-of-solar-indices/> ,Accessed on August 2021
- [23] NMBD event search tool. <https://www.nmdb.eu/nest/>
- [24] T. Renkowitz and R. Latteck [2019], "On improving radar echo spectral width analysis for atmospheric turbulence estimates," 2019 International Interdisciplinary PhD Workshop (IIPHDW), 2019, pp. 19-23, 10.1109/IIPHDW.2019.8755421
- [25] Balsley, B.B., Gage, K.S [1980]. The MST radar technique: Potential for middle atmospheric studies. PAGEOPH 118, 452–493. <https://doi.org/10.1007/BF01586464>
- [26] Nath, N., Setty, C.S.G.K [1976]. The D-region ion composition. PAGEOPH 114, 891–908. <https://doi.org/10.1007/BF00876189>
- [27] P.M Banks, G. Kockarts [1973] :Formation of the ionosphere. In: Aeronomy chapter 17,101-123,<https://doi.org/10.1016/B978-0-12-077802-7.50009-9>
- [28] Bauer S.J. [1973] Models of Planetary Ionospheres. In: Physics of Planetary Ionospheres. Physics and Chemistry in Space, vol 6. Springer, Berlin, Heidelberg.  
[https://doi.org/10.1007/978-3-642-65555-5\\_7](https://doi.org/10.1007/978-3-642-65555-5_7)
- [29] Thomas [1974]: Composition and Chemistry (327-334) . In: Aeronomy of the Middle Atmosphere. Atmospheric and Oceanographic Sciences Library, vol 32. Springer, Dordrecht. [https://doi.org/10.1007/1-4020-3824-0\\_5](https://doi.org/10.1007/1-4020-3824-0_5)
- [30] Chu, Yen-Hsyang, [2003], "Radial velocity and doppler spectral width of echoes from field-aligned irregularities localized in the sporadic E region" Journal of Geophysical Research Vol. 108, No. A7, 0148-0227. [https://doi.org/10.1175/1520-0426\(2002\)019<1955:BBE00M>2.0.CO;2](https://doi.org/10.1175/1520-0426(2002)019<1955:BBE00M>2.0.CO;2)
- [31] Latteck, R., Renkowitz, T., and Strelnikov, B. [2019]: D region observations by VHF and HF radars during a rocket campaign at Andoya dedicated to investigations of PMWE, Adv. Radio Sci., 17, 225–237, <https://doi.org/10.5194/ars-17-225-2019>.
- [32] Srinivas Rao, V.K. Anandan, P. Narasimha Reddy [2008]: Evaluation of DBS wind measurement technique in different beam configuration for a VHF wind profiler, Journal of Atmospheric and ocean technology, 2304-2312  
<https://doi.org/10.1175/2008JTECHA1113.1>
- [33] Ronald F.Woodman and Alberto Guillen [1974]: Radar observation of winds and turbulence in the stratosphere and mesosphere:Journal of atmospheric science 493-505.  
[https://doi.org/10.1175/15200469\(1974\)031<0493:ROOWAT>2.0.CO;2](https://doi.org/10.1175/15200469(1974)031<0493:ROOWAT>2.0.CO;2).

- 
- [34] Wilhelm s, Stober G, Chau JL [2017]: A comparison of 11 year mesospheric and lower thermospheric winds determined by the meteor and MF radar at 69°N, *Ann.Geophys.*,35,893-906, <https://doi.org/10.5194/angeo-35-893-2017>.
- [35] Calisto, Marco [2011]: Influence of energetic particle precipitation on atmospheric chemistry and climate. <https://doi.org/10.3929/ethz-a-006382983>.
- [36] M.J. Beharrell, F. Honary, C.J. Rodger and M.A. Cilverd [2015]: Substorms induced energetic electron precipitation: Morphology and prediction, *J. Geophys. Res. Space Physics*, 120, 2993-3008, <https://doi.org/10.1002/2014JA020632>.
- [37] Toralf Renkwitz, Masaki Tsutsumi, Fazlul I.Laskar, Jorge L.Chau & Ralph Latteck[2018]: On the role of anisotropic MF/HF scattering in mesospheric wind estimation. *Earth Planets Space* 70, 158 (2018).1002/2015GL065523. <https://doi.org/10.1186/s40623-018-0927-0>

---

## **Acknowledgment**

I would like to express my sincere gratitude and warm appreciation towards all personages who have helped me in this endeavor.

I acknowledge with a deep sense of reverence, my sincere thanks to Prof. Andreas Ahrens for being my first supervisor and for being sources of inspiration in the classes taught. I am highly obliged for the best guidance offered by him throughout my master studies.

I am extremely thankful and pay my heartfelt obligation to Dr. Toralf Renkwitz for his valuable guidance and support for the completion of my thesis. Without his active guidance, help and encouragement, I would not have made headway in the project. His unwavering enthusiasm towards the subject kept me constantly engaged with my thesis, and his personal generosity helped make my time at IAP valuable. It was a great honor to finish this work under his supervision.

I would like to give my special thanks to Prof. Dr. Jorge L. Chau and Prof. Dr. Franz Josef Lübken for offering me the opportunity to do my thesis in IAP, Kühlungsborn.

At last but not least gratitude goes to all of my friends in IAP.

---

## **Statement of Authorship**

I, Archana Vijayalekshmi Harikumar hereby declare that I completed this work independently and that I have used no aids other than those referenced.

The part of the work, which includes phrases or points taken from other sources, are clearly marked with the origin of the information. This also applies to diagrams, sketches, visual representations as well as for sources from the internet.

I also declare that I have not submitted this work in any other testing procedure as an examination paper, nor will I in the future.

The submitted written version matches the version stored on the data medium.

Wismar, 27.10.2021

(Signature)